



UPPSALA  
UNIVERSITET

*Digital Comprehensive Summaries of Uppsala Dissertations  
from the Faculty of Science and Technology 1380*

# Electron tomography analysis of 3D order and interfacial structure in nano-precipitates

LING XIE



ACTA  
UNIVERSITATIS  
UPSALIENSIS  
UPPSALA  
2016

ISSN 1651-6214  
ISBN 978-91-554-9590-9  
urn:nbn:se:uu:diva-284102

Dissertation presented at Uppsala University to be publicly examined in Polhemssalen, Ångströmlaboratoriet, Lägerhyddsvägen 1, Uppsala, Tuesday, 14 June 2016 at 13:00 for the degree of Doctor of Philosophy. The examination will be conducted in English. Faculty examiner: Professor Christian Kübel (Electron Microscopy and Spectroscopy Laboratory, Karlsruhe Institute of Technology).

### Abstract

Xie, L. 2016. Electron tomography analysis of 3D order and interfacial structure in nano-precipitates. *Digital Comprehensive Summaries of Uppsala Dissertations from the Faculty of Science and Technology* 1380. 84 pp. Uppsala: Acta Universitatis Upsaliensis. ISBN 978-91-554-9590-9.

Structural characterization is essential to understand the formation mechanisms of the nanostructures in thin absorber layers in third generation solar cells and amyloid protein aggregates. Since the dimension of the precipitated structures is in nanometer scale, electron tomography technique in transmission electron microscopy (TEM) has been applied as a major tool to analyze the 3D order and distribution of precipitates using the electron tomography technique.

Silicon rich silicon carbide (SRSC) films were deposited by plasma enhanced chemical vapor deposition (PECVD) technique and annealed in the nitrogen atmosphere for 1 hour at 1100 °C. The spectrum-imaging (SI) technique in Energy filtered TEM (EFTEM) imaging mode was used to develop electron tomography. From the reconstructed sub-volumes, the complex, three dimensional interfacial nanostructure between the precipitated NPs and their parental matrix was observed and explained in terms of thermodynamic concepts. Additionally, the feasibility of raw data 4D electron tomography has been demonstrated using the EFTEM SI dataset.

The aggregation process of the human islet amyloid polypeptide (hIAPP) has a great impact on human health. In this thesis, a model system has been taken to study the ultrastructure of the hIAPP aggregates that are present in the fat body tissue surrounding the brain of *Drosophila melanogaster*. Electron tomography technique on TEM revealed clear crystalline structures in 3D. For the first time, the presence of a 5-fold twinned structure in biology was discovered. An intriguing finding is the filament like interconnection of hIAPP protein granules observed predominantly along the nearest neighbor directions. This suggests the existence of the directional binding forces between two nearest protein granules in addition to dipole-dipole interactions.

**Keywords:** Electron tomography, nanoprecipitate, interfacial structure.

*Ling Xie, Department of Engineering Sciences, Applied Materials Sciences, Box 534, Uppsala University, SE-75121 Uppsala, Sweden.*

© Ling Xie 2016

ISSN 1651-6214

ISBN 978-91-554-9590-9

urn:nbn:se:uu:diva-284102 (<http://urn.kb.se/resolve?urn=urn:nbn:se:uu:diva-284102>)

*Dedicated to my family*



# List of Papers

This doctoral thesis consists of the following papers, which are referred to in the text by their Roman numerals. Reprints of the published papers were made with permission from the publishers.

- I**                    **Indium tin oxide-silicon nanocrystal nanocomposite grown by aerosol assisted chemical vapour deposition.**  
O'Brien S., Linehan K., Doyle H., Kingsley A., Ashfield C., Frank B., Xie L., Leifer K., Thony P., Perraud S., Pemble M. E., Povey I. M.  
*J. Sol-Gel Sci. Technol.*, 2015, **73**, 666–672.
- II**                    **Nanocrystal size distribution analysis from transmission electron microscopy images**  
M. van Seville, L. J. P. van der Maaten, L. Xie, K. Jarolimek, R. Santbergen, R. A. C. M. M. van Swaaij, K. Leifer and M. Zeman.  
*Nanoscale*, 2015, **7**, 20593–20606.
- III**                    **Optoelectronic properties of p-i-n heterojunctions based on germanium nanocrystals**  
S. Parola, E. Quesnel, V. Muffato, L. Xie, K. Leifer, J. Coignus and A. Slaoui.  
*J. Appl. Phys.*, 2013, **114**.
- IV**                    **Silicon nanocrystals on amorphous silicon carbide alloy thin films: Control of film properties and nanocrystals growth**  
J. Barbe, L. Xie, K. Leifer, P. Faucherand, C. Morin, D. Rapisarda, E. De Vito, K. Makasheva, B. Despax and S. Perraud.  
*Thin Solid Films*, 2012, **522**, 136–144.

- V**                    **Silicon nanocrystals: Novel synthesis routes for photovoltaic applications**  
S. Perraud, E. Quesnel, S. Parola, J. Barbe, V. Muffato, P. Faucherand, C. Morin, K. Jarolimek, R. A. C. M. M. Van Swaaij, M. Zeman, S. Richards, A. Kingsley, H. Doyle, K. Linehan, S. O'Brien, I. M. Povey, M. E. Pemble, L. Xie, K. Leifer, K. Makasheva and B. Despax.  
*Phys. Status Solidi a-Applications Mater. Sci.*, 2013, **210**, 649–657.
- VI**                    **Bonding symmetry and structural analysis of the hIAPP protein aggregates using the electron tomography technique**  
Ling X., Kenta O., Xiaohong G., Gunilla T. W. and Klaus L.  
*Submitted.*
- VII**                    **Electron tomography analysis of the interfacial nanostructures between the Si networks and SiC nanoparticles in the thermally annealed Si rich SiC films**  
Ling X., Karol J., Rene A. C. M. M. V. S., Vancho K., Jan R. and Klaus L.  
*In manuscript.*

Reprints were made with permission from the respective publishers.

# Contents

1.	Introduction .....	11
1.1.	Solar cells .....	11
1.2.	Third generation solar cells .....	12
1.3.	The nucleation and growth and spinodal decomposition .....	15
1.4.	hIAPP protein aggregates in the fat body of the <i>Drosophila melanogaster</i> .....	18
1.5.	The development of electron tomography .....	20
2.	Synthesis and analysis of PV absorber layer .....	23
2.1.	The deposition of the absorber layers .....	23
2.2.	Transmission Electron Microscopy .....	25
2.2.1.	Sample preparation for TEM .....	30
2.2.2.	Contrast optimization of NPs in the investigated samples .....	32
2.3.	Additional characterization techniques .....	37
2.3.1.	Ion beam analysis .....	37
2.3.2.	Raman spectroscopy .....	38
2.4.	Conclusion .....	40
3.	Electron tomography on TEM .....	41
3.1.	The acquisition of the tilt series .....	41
3.2.	Alignment .....	44
3.3.	Reconstruction .....	45
3.4.	Segmentation and post processing .....	50
3.5.	Conclusion .....	51
4.	Electron tomography analysis on the absorber layer of all-Si tandem solar cells .....	53
4.1.	Bright field tomography .....	53
4.2.	EFTEM SI tomography .....	56
4.3.	4D electron tomography .....	59
4.4.	Conclusion .....	64

5.	Electron tomography analysis on the hIAPP protein aggregates.....	65
5.1.	3D crystalline structural analysis.....	65
5.2.	Single particle analysis of hIAPP protein granules .....	67
5.3.	Conclusion.....	69
6.	Conclusions and outlook.....	70
	Acknowledgements.....	72
	Summary in Swedish .....	74
	Bibliography .....	77



# Abbreviations

2BC	Two-Beam Case
3D	Three Dimensional
4D	Four Dimensional
AACVD	Aerosol Assisted Chemical Vapor Deposition
APT	Atom Probe Tomography
A $\beta$	Amyloid Beta peptide
BF	Bright Field
BCT	Body Centered Tetragonal
CCD	Charge-Coupled Device
CVD	Chemical Vapor Deposition
EELS	Electron Energy-Loss Spectroscopy
EFTEM	Energy Filtered Transmission Electron Microscopy
ERDA	Elastic Recoil Detection Analysis
FCC	Face-Centered Cubic
FEG	Field Emission Gun
FWHM	Full Width at Half Maximum
GIF	Gatan Image Filter
HCP	Hexagonal Close-Packed
hIAPP	human Islet Amyloid Polypeptide
HRTEM	High Resolution Transmission Electron Microscopy
LPCVD	Low Pressure Chemical Vapor Deposition
NP	Nanoparticle
PV	Photovoltaic
PECVD	Plasma Enhanced Chemical Vapor Deposition
SAD	Selected Area Diffraction
SART	Simultaneous Algebraic Reconstruction Technique
SI	Spectrum Imaging
SIRT	Simultaneous Iterative Reconstruction Technique
SRSO	Silicon Rich Silicon Oxide
SRSC	Silicon Rich Silicon Carbide
STEM	Scanning Transmission Electron Microscopy
TEM	Transmission Electron Microscopy
ZLP	Zero-Loss Peak



# 1. Introduction

Precipitation refers to a process that creates a solid (called as “precipitate”) from a supersaturated solid or liquid solution <sup>1,2</sup> or vapors <sup>3</sup>. The most common forms of precipitates include clouds, drizzle, rain, sleet, snow and hail, which are the products of the condensation of supersaturated atmospheric water vapors and then falls by gravity. In materials science, the precipitation may occur when the concentration of a solute exceeds its solubility and can be rapidly induced in a variety of ways such as raising the temperature, removing the solvent by evaporation, adding another solvent or solutes or even the combinations of these. In life science, the precipitation process is widely used to purify the proteins and eliminate contaminants <sup>4</sup>. The precipitation of the amyloid peptides in the body is due to their remarkable low solubility or insolubility in aqueous conditions. The self-assembled aggregation process of the precipitated amyloid peptides leads to the formation of large and insoluble amyloid deposits that are associated with a number of diseases <sup>5,6</sup>. The degree of control over the morphology of the precipitates from the matrix is minor and the understanding of the interfacial structure between the precipitates and the surrounding matrix in all three dimensions (3D) with nanometer resolution is not well documented experimentally.

In this thesis, the electron tomography technique on transmission electron microscopy (TEM) was applied to characterize the 3D nanostructures formed in both the materials science and life science samples. Surprisingly, the life science sample which contains amyloid peptides protein aggregations has a highly crystalline structure, while the nanostructures observed in the materials science sample have very complex morphologies. In particular, the analysis on the interfacial nanostructures in 3D was addressed in this thesis and the formation of the interfacial nanostructures is correlated to the formation mechanism of corresponding nanostructures. In turn, the understanding of atomic scale order and 3D nanostructure gives new insights in the origin of materials properties of these complex systems.

## 1.1. Solar cells

Energy is a central element for the social and economic development. During the past 50 years (1965-2014), global primary energy consumption continues to grow, though there are signs that the growth rate becomes slower in 2014, especially for the consumption of fossil fuels <sup>7</sup>. This is due to a combination of factors, such as the persisted high energy prices, the increase in pollution to troublesome levels, the end of double digit economic growth in China and the emerging of alternative renewable energies. New renewable energies (solar, wind, geothermal, biofuels, hydropower, ocean energy, etc) seize about 0.87 % of total global primary energy consumption in 2004, and by 2014 it had grown to 2.98 % <sup>7</sup>. Among these renewable energies, wind

turbines are normally located in the rural areas rather urban, because they take space and can be noisy; hydropower is typically generated by building dams which usually take more areas than building wind turbines, and also dams are expensive to build and keep the maintenance; the efficiency of biofuels is relatively low; geothermal is strongly location dependent; thus, solar energy is more versatile and highly attractive compared with other renewable energies.

Nowadays, there are two ways to transform the solar energy into electricity. The first method is to use the thermo-solar power system to thermodynamically produce electricity<sup>8</sup>. The second method is to use solar photovoltaic (PV) cells to electronically convert the solar energy into a flow of electrons to generate electricity. Research activities to improve the conversion efficiency, reliability and scalability of solar cells have been active more than 60 years<sup>9</sup>. In the past 60 years, the PV technologies have experienced three generations. The first generation of solar cells is based on single crystalline silicon (Si) or III-V alloys. This generation of solar cells consists of single p-n junction and has a typical conversion efficiency of 20 %. Although this generation of technology requires high production energy and labor forces, it is still dominating the commercial market due to its high stability and good conversion efficiency. Compared with the first generation solar cells, second generation solar cells have been developed to address the lower fabrication energy and production costs. The major difference from the first generation solar PV cell is the thickness of the absorber layer which can be just few microns for second generation solar cells, while the thickness of the absorber layer of the first generation cells is about hundreds of microns. Thus, it was also called as thin film solar cells based on the multiple absorber compounds, such as CdTe (Cadmium-Telluride) and CIGS (Copper-Indium-Gallium-Selenide). The alternative examples of the low cost solar cells are dye-synthesized solar cells and organic solar cells. The typical conversion efficiency is about 10% for second generation solar cells.

## 1.2. Third generation solar cells

The third generation solar cells were designed as to combine the both virtues of the first and second generation solar cells, such as high efficiency and low costs. To reach this goal, a number of different novel syntheses methods have been suggested to fabricate the absorber layer for third generation solar cells, the core concept is to tune the fluorescence (optimize the absorption of the incoming light) by controlling the nanostructures formed inside the absorber layer under different synthesis conditions.

The promising approach to enhance the absorption efficiency of third generation cells is to fabricate a stack of absorber layers, where each layer has a

band gap which is optimized for the absorption of one wavelength range in the solar spectrum. For example, the theoretical efficiency of bulk Si based solar cells is limited by 29%, because of the transmission of photons with energies lower than the Si band gap (1.12 eV) and incomplete use of photons with energies higher than the Si band gap. However, the theoretical efficiency increases to 42.5% by adding an absorber layer having 1.8 eV band gap, and to 47.5% by adding two absorber layers having 1.5 eV and 2 eV band gaps on top of the bulk Si cell. Such a Si based multilayer solar cell is also call as “all-Si” tandem solar cell. Since the band gap of Si is tunable, when the size of the Si-entities is in the nanometer range (size less than 10 nm) due to the quantum confinement effect. Layers containing Si nanoparticles (NPs) with different sizes embedded in SiO<sub>2</sub>, Si<sub>3</sub>N<sub>4</sub> or SiC matrix should have different band gaps. These layers can be chosen as an absorber layer for “all-Si” tandem solar cells. From the technological point of view, the efficiencies of Si NPs based third generation solar cells will be greatly influenced by two parameters: (i) the size and spacing of Si NPs in 3D, (ii) the interface between the precipitated NPs and the surrounding matrix <sup>10</sup>.

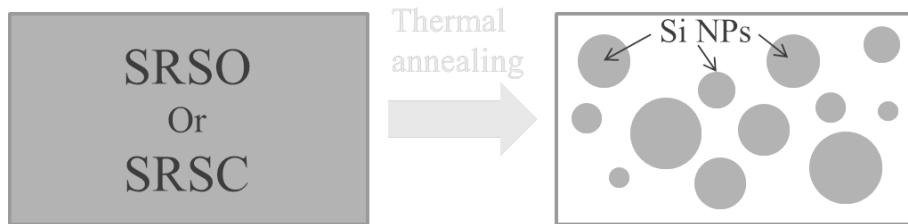


*Figure 1: Schematic of thermal activated precipitation processing of Si NPs in Si rich Si Oxide (SRSO) or Si rich Si Carbide (SRSC) films. Layers with Si excess are deposited with sub-stoichiometric and Si NPs are precipitated from the matrix.*

The State of the Art processes to fabricate the absorber layers which contain Si NPs embedded in the matrix are based on two steps as illustrated in **Figure 1**: (i) the deposition of a thin film which is usually non-stoichiometric and has the excess Si in the thin film, (ii) the excess Si precipitate into Si NPs through the high temperature annealing process. The formation of Si NPs in oxide and nitride matrixes has been demonstrated firstly by M. Green and co-workers, from the University of New South Wales in Australia <sup>11</sup>. The quantum confinement effect has been demonstrated by photoluminescence (PL) measurements, as the PL energy increasing by the decreasing of the Si NPs size <sup>12</sup>. The determination of the size and morphology of the precipitated Si NPs in 3D was firstly performed by means of the electron tomography technique on TEM using the energy filtered TEM (EFTEM) sig-

nals and the Si NP presented in the Si rich Si Oxide (SRSO) matrix seems to have a non-spherical shape<sup>13</sup>.

Besides the size and morphology of the precipitated Si NPs, the spacing between the adjacent Si NPs has been considered as another important parameter which can influence the transport properties of the excited carriers<sup>14</sup>. In order to have a high possibility for carriers to transport between two adjacent Si NPs, one can either fabricate the Si NPs close enough so that the wave function of NPs overlap or choose a matrix materials having a low barrier height (defined as the energy difference between the confined energy level of NPs and the conduction band edge of the matrix)<sup>15</sup>. It was calculated that Si NPs would have to be separated by no more than 1~2 nm in SRSO for a reasonable overlap of the wave function to generate conductivity due to high energy barrier of SiO<sub>2</sub> (~ 3.2 eV)<sup>15</sup>. Thus, the analysis on the 3D morphology and spacing between the precipitated Si NPs has become an appealing research topic in the field of the Si NPs based absorber layer synthesis. In last 10 years, 3D imaging techniques with nanometer resolution, such as electron tomography on TEM combined with atom probe tomography (APT), were applied to precisely determine the 3D distribution of NPs (**Table 1**).

After the 3D analysis, one can classify the morphologies of Si nanostructures into three different classes, in each of them we may expect a different carrier transport mechanism. The classes are:

1. Non-spherical Si NPs isolated and uniformly dispersed in the matrix<sup>16,19,20</sup>
2. Some of non-spherical Si NPs starts to connect with their nearest neighbors<sup>13</sup>
3. All the Si NPs are connected to form a network like structure<sup>17,18,19,20</sup>

From the **Table 1**, one can see that the morphology of Si nanostructures (either isolated NPs or network) were less dependent on the annealing conditions (temperatures, durations and atmospheres), but strongly correlated with the excess Si content. When the excess of Si content is below 30 at. % (16 vol. %), then the isolated Si NPs can be obtained. If the excess of Si content is above 30 at. %, then the excess Si will form network like structures in the SiO<sub>2</sub> matrix. From the listed references in **Table 1**, the formation mechanisms of the isolated Si NPs or the Si network like structures were explained in terms of thermodynamic concepts: the classic nucleation and growth (Si < 30 at. %) and spinodal decomposition (Si > 30 at. %).

Annealing temperature (°C)	Durations	The excess Si (at. %)	Atmospheres	3D Si Morphology	References
900	1 hour	25	N2	Isolated NPs	16
900	1 hour	30	N2	Network	16
1000	30 seconds	50	Ar	Network	17
1100	30 seconds	50	Ar	Network	17,18
1150	30 seconds	50	Ar	Network	17
950	30 minutes	8	N2	Isolated NPs	19,20
950	30 minutes	18	N2	Isolated NPs	19,20
950	30 minutes	32	N2	Network	19,20

*Table 1. The observed Si nanostructures in three dimensions embedded in the SRSO as a function of the excess Si and different annealing conditions (temperatures, durations and atmospheres). The 3D morphology of Si nanostructures was determined by electron tomography and APT techniques.*

### 1.3. The nucleation and growth and spinodal decomposition

There are two types of phase transitions in the solid or liquid solution when the system is not reaching the thermodynamic equilibrium condition. First, the classic nucleation and growth is a process which has been described as two steps: the nucleation<sup>21,22</sup> and the Ostwald ripening<sup>23</sup> as shown in **Figure 2**. Second, it is the spinodal decomposition which refers to a process that a binary alloy or compound decomposes into two phases that are fluctuating spatially as sinusoidal compositional profile<sup>24</sup>.

The nucleation is always associated with metastability and relatively large compositional fluctuation so that it can overcome the energy barrier to form a nucleus. The nuclei above the critical size can grow further and those below the critical size will be dissolved by larger precipitates, this is called as Ostwald ripening or coarsening effect. The critical size of the nuclei is determined by the surface tension at the interface between the precipitates and the surrounding matrix<sup>25</sup>. Depending on the formation mechanisms, the

evolution of the precipitate size as a function of solute concentration and time is described in **Figure 2** <sup>26</sup>.

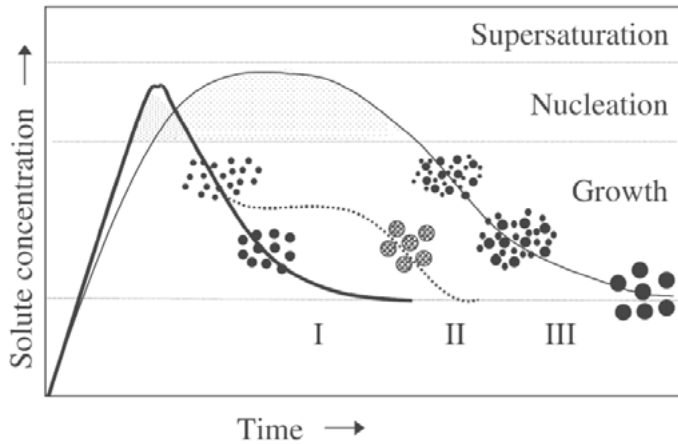


*Figure 2: Mechanism of formation of uniform particles in solution: curve I: single nucleation and uniform growth by diffusion (classical model of LaMer and Dinegar); curve II: nucleation, growth and aggregation of smaller subunits; curve III: multiple nucleation events and Ostwald ripening growth. Reproduced from J. Phys. D. Appl. Phys. 36, R182–R197. Copyright © 2003, IOP Publishing Ltd. [26]*

In principle, there are three possible formation mechanisms to obtain uniform size distribution of precipitates in solutions as shown in **Figure 2**: (i) the homogenous nucleation and growth process (curve I in **Figure 2**); (ii) the aggregation of smaller precipitated subunits (curve II in **Figure 2**); (iii) the heterogeneous nucleation and growth process (curve III in **Figure 2**). The homogenous nucleation and growth happens spontaneously and randomly without preferential nucleation sites, while the heterogeneous nucleation and growth occurs at preferential sites, such as grain boundaries, dislocations or impurities <sup>27</sup>. The precipitation of Si NPs from the their parental matrix always follows the heterogeneous nucleation and growth model that leads to a broadened size distribution of precipitates described by the Ostwald ripening process <sup>28</sup>. The growth of the precipitated NPs always needs to grab solute atoms from the surrounding matrix, thus, a concentration gradient of the solute atoms around the interface of the precipitated NPs is always expected <sup>29</sup>. In **Paper VII**, the observation of the interfacial nanostructure was explained by the nucleation and growth theory.

The spinodal decomposition refers to a process where a binary alloy or compound decomposes into two phases which are fluctuating as sinusoidal compositional profile <sup>24</sup>. In contrast to the nucleation and growth process, there is



no energy barrier to initiate the spinodal decomposition process. The whole decomposition process can be described as two stages: first, a fluctuation of composition forms but small in amplitude and large in extent; secondly, the compositional fluctuation increases exponentially until reach the limit which is set by the miscibility gap<sup>30</sup>. As the annealing proceeding, the coarsening of the composition increases making the wavelength of the compositional fluctuation larger than the initial stage, but the concentration of the decomposed phase can remain the same, where a typical wavelength is about 5 nm<sup>31</sup>. The 3D morphological evolution during the spinodal decomposition process was simulated by taking a binary alloy as examples, it reveals that isolated NPs can be formed in the initial stage of the spinodal decomposition process, and a highly interconnected columnar like structure along the Z direction can be seen in the later stage of the spinodal decomposition process<sup>32</sup>. The simulated 3D temporal morphology evolution is in good agreement with the finding presented in **Paper VII**.

By knowing the formation mechanisms of the nanostructures in the matrix, let us come back to the description on the 3D spacing of Si NPs in SiO<sub>2</sub> matrix. As mentioned, it is important to have small spacing (1~2 nm) of Si NPs in order to obtain the good transport properties of carriers. From the **Table 1**, we learned that when the excess Si content is less than 30 at. %, the nucleation and growth process govern the formation of isolated Si NPs. Assuming a homogenous nucleation and growth takes place for all the isolated Si NPs and all the Si NPs are distributed into a close packed order (FCC or HCP), then only when the isolated Si NPs have a radius of 0.68 nm with a center to center distance of 1.41 nm, they can take a volume fraction of 16 vol. %. This is difficult to achieve, because small size of NPs (below the critical size) may not be stable in the matrix materials<sup>25</sup>. In the case of Si NPs are formed as embedded NPs in a Si network structure, the energy barrier between the crystalline Si (c-Si) and amorphous Si (a-Si) is about 0.1~0.2 eV<sup>33</sup>, which is lower compared with the case of Si NPs embedded in the SiO<sub>2</sub> matrix (~ 3.9 eV). In the Si network like structure, the center to center spacing between Si NPs can be 9 nm (this value was calculated by using the formula in [15], taking the electron effective mass in Si of 0.19m<sub>0</sub><sup>34</sup>) and the carriers are transported by migration instead of tunneling<sup>35</sup>.

Compared to the SRSO films, Si NPs embedded in a SRSC matrix are particularly interesting because of the lower barrier height of SiC relative to SiO<sub>2</sub><sup>36</sup>. In the SiC matrix, in order to have good electronic transport properties, the spacing between Si NPs can be more than 4 nm due to the lower barrier height<sup>15</sup>. However, experimental investigations on the nanostructures formed in SRSC films are few<sup>37,38,39</sup>, and 3D characterization on the nanostructures and interfacial structures formed in such films were not carried out yet.

## 1.4. hIAPP protein aggregates in the fat body of the *Drosophila melanogaster*

In life science, proteins are one of the major biological macromolecule assemblies, for example, enzymes, toxins, hormones, antibodies and peptides<sup>40</sup>. These macromolecule assemblies are of interest in many research and industrial fields and the detailed structural analysis of macromolecule assemblies provides new possibilities for the design of new medicines and engineered molecules with improved properties<sup>41</sup>. The native protein macromolecules are generally difficult to aggregate into crystalline structures, because the inter- and extracellular environment are normally quite crowded with other molecules<sup>42</sup>. For example, there are maybe other types of fluid assemblies in the pathway of free diffusion of the protein macromolecules so that harbor the crystallization process<sup>42</sup>.

The curve II in **Figure 1** can best describe the aggregation process of protein macromolecules that usually contains two steps. The first step is the precipitation of supersaturated protein macromolecules; the second step is the aggregation of the precipitated protein macromolecules. Thermodynamically, the precipitation of protein macromolecules is not very different from the precipitation process of Si NPs from the SRSO or SRSC films. In both cases, a supersaturated condition of protein macromolecules or Si atoms is achieved in the initial state. The difference is that the growth of Si NPs is activated by thermal diffusion of Si atoms, in the case of proteins, heating is not a general method to facilitate the precipitation of the protein macromolecules, because most of proteins may quickly denature at high temperatures. In this thesis, the targeted protein macromolecule is one of the amyloid polypeptide families, human Islet Amyloid Polypeptide (hIAPP). The aggregation of the precipitated hIAPP leads to the formation of hIAPP aggregates in the human body which is believed to be associated with Type II Diabetes<sup>43</sup>.

Until now, 27 types of protein molecules were detected that can form amyloid aggregations leading to various diseases<sup>43</sup>. The aggregation process of these amyloid protein molecules are known to be associated with a large number of diseases, such as Alzheimer's disease and type II diabetes (**Table 2**). Both of these diseases are associated with amyloid-like fibril formation. However, the protein fibrils causing Parkinson's disease and Huntington's disease do not share some of the common characteristic features of amyloid classification, the protein molecules in these three cases are called as amyloid-like proteins molecules, and the other protein molecules are called as amyloid protein molecules<sup>43,44</sup>. The definition of amyloid was not clear until 2007<sup>43</sup>.

<b><i>Disease</i></b>	<b><i>Protein molecules</i></b>
Alzheimer's disease	A $\beta$ <sup>43</sup> , Tau <sup>43</sup>
Amyotrophic lateral sclerosis	Superoxide dismutase 1 <sup>45</sup>
Huntington's disease	Huntingtin <sup>45</sup>
Parkinson's disease	$\alpha$ -Synuclein <sup>45</sup>
Spongiform encephalopathies	Prion protein <sup>45</sup>
Familial amyloidotic polyneuropathy	Mutant Transthyretin <sup>43</sup>
Senile systemic amyloidosis	Wildtype Transthyretin <sup>43</sup>
Type II Diabetes	human Islet amyloid polypeptide <sup>43</sup>

*Table 2. Amyloid and amyloid like diseases and the related protein molecules.*

In 1927, it was found that an apple-green birefringence is emitted under the polarized light after the amyloid deposits bind to Congo red<sup>46</sup>. In 1959, the first TEM image on the amyloid deposits shows a characteristic fibrous appearance under high magnification<sup>47</sup>. This observation initiated the structural investigation of the amyloid fibril, and from the X-ray diffraction patterns, the amyloid fibrils were characterized by two distinct signals: a sharp reflection signal at 4.7 Å which corresponds to the spacing between the  $\beta$ -sheets in the protofilament, and a more diffuse reflection signals at 10 Å - 11 Å which corresponds to the spacing between the protofilaments<sup>48</sup>. Nowadays, the amyloid is defined as protein deposits found *in vivo*, having following three characteristics: (i) fibrous appearance under the electron microscopy; (ii) a typical X-ray diffraction pattern; (iii) apple-green birefringence under plane polarized light when amyloid binds to Congo red.

The *Drosophila melanogaster* has been used as a model to study the neurodegenerative diseases, for example, Alzheimer's disease<sup>49,50</sup> and Huntington's disease<sup>51</sup>. The use of *Drosophila melanogaster* model has certain advantages<sup>52</sup>: (i) well-defined genetic characteristics; (ii) large quantities of flies can be easily prepared; (iii) short lifespan. The analysis on the *Drosophila melanogaster* genome has revealed that 77 % of human disease related genes have a homologue in *Drosophila melanogaster*<sup>53</sup>. A database called "Homophila" in 2001 lists all human disease related genes in *Drosophila melanogaster*<sup>54</sup>. Therefore, the *Drosophila melanogaster* can be used as a model to study the amyloid associated human disease.

During the last decade, TEM has been applied as a main instrument to resolve the detailed structural information on amyloid or amyloid like fibrils taken from human tissue samples <sup>47</sup>, because the protein precursors of amyloid or amyloid like fibrils that may vary in size in their primary and secondary structures, they assemble into similar fibrous structures <sup>55</sup>. The electron tomography technique on TEM enables a detailed 3D analysis on a subcellular level <sup>56,57</sup>, in this thesis, the electron tomography technique was applied to study the 3D distribution of the hIAPP aggregates formed at the fat body tissue in the *Drosophila melanogaster*.

## 1.5. The development of electron tomography

The analysis on the 3D structure of nano-precipitates can provide valuable information to understand the formation mechanism of nanostructures in the material systems described above, the NP based third generation solar cells and the hIAPP protein aggregates. The electron tomography technique on TEM has been developed for the characterization of 3D morphological, chemical and structural imaging with a resolution in nanometer or even down to the atomic resolution.

Electron tomography is a 3D imaging technique which use the contrast mechanisms generated in a TEM as basis for tomographic reconstruction. In this thesis, as electron tomography has been applied as a major technique to answer the materials related questions, a detailed description of contrast mechanism in TEM, sample preparation and the principles for the tomographic reconstruction is given in **Chapter 2 and 3**. Here, in this chapter, the historical development of electron tomography with the key technical advances has been roughly reviewed.

Historically, the first electron tomography results were published in the year of 1968 <sup>58-60</sup>. Based on the x-ray crystallographic knowledge, Hoppe and colleagues has retrieved 3D structural information from a number of electron micrographs <sup>58</sup>. Hart has demonstrated a method to improve the signal to noise ratio of a tilt series acquired from a unstained biological material at high resolution <sup>59</sup>. By taking the advantage of the helical symmetry of the targeted biological macromolecule, De Rosier and Klug has obtained a 3D reconstruction of a negatively stained bacteriophage T4 tail using a single projection <sup>60</sup>. Until the 1990s, the spreading of electron tomography technique was limited by the computational power involved in the tomographic reconstruction. In the beginning of 1990s, the implementation of charge coupled device (CCD) cameras into the computer-controlled TEMs became affordable for a larger microscopy society. This made the fully automated image acquisition and complex data processing possible for electron tomography <sup>61-63</sup>. Before the end of 1990s, the applications of electron tomography

were almost exclusively focused in life sciences <sup>64</sup>. The transfer of electron tomography technique to materials science field occurred relatively late due to the projection requirement <sup>65</sup>. For biological applications, conventional bright field TEM (BFTEM) images can be used as projections for tomographic reconstruction since the contrast in BFTEM images reflects the mass and density of material in biological samples. On the other hand, the samples from materials science always contain crystalline structures. In the BFTEM imaging mode, the diffraction contrast is dominant, making the tomographic reconstruction unreliable or even impossible. Several other imaging techniques on TEM have been proposed as a general solution for the development of electron tomography on crystalline samples <sup>66,67</sup>. These imaging techniques include high angle annular dark field (HAADF) in scanning TEM (STEM) mode <sup>66,67</sup>, energy filtered TEM (EFTEM) using electron energy loss spectroscopy (EELS) signal <sup>68,69</sup> and energy dispersive x-ray spectroscopy (EDS) mapping <sup>70,71</sup>. In the STEM HAADF imaging mode, the electrons incoherently and elastically scattered to large angles are collected to form images. The contrast seen in such images is dominated by atomic numbers due to the Rutherford scattering. In the EFTEM imaging mode, the inelastically scattered electrons are detected that fulfill at least to a good approximation of the projection requirement for thin samples <sup>67</sup>.

When it comes to 2000s, electron tomography has been adopted rapidly by materials scientists as an important tool to study 3D morphologies and chemical compositions of nanostructures <sup>66</sup>. Many different types of nanostructures were investigated by electron tomography in many fields. For example, electron tomography technique was applied to obtain 3D elemental maps of different elements present in the SiC pore oxidation with nanometer resolution <sup>72</sup>; Z contrast based electron tomography was used to determine the structure of nanocatalysts <sup>73</sup> and octapods shaped NPs <sup>74</sup>; in order to reduce the missing wedge effect, dual tilting series was used to investigate the tetrapod shaped NPs <sup>75</sup>; the core-shell nanoplasmonic structure <sup>76</sup> and palladium NPs with complex shapes <sup>77</sup> were revealed by electron tomography. For the NPs based SRSO films, the determination of the morphology of the precipitated Si NPs was firstly performed by means of EFTEM signals and the Si NPs precipitated in the SRSO matrix seem to have a non-spherical shape <sup>13</sup>. By including the prior knowledge on the morphology of the targeted sample, discrete tomography was introduced to reconstruct nano-object with improved resolution <sup>78</sup>.

Most recently, four dimensional (4D) electron tomography has been demonstrated as a powerful technique to probe the elemental, physical and chemical information of a material in three dimensions <sup>70,79–82</sup>. Gass and coworkers have applied 4D electron tomography technique to study the interfacial structural and chemical composition of the multi-walled carbon nanotubes

and nylon composite<sup>82</sup>. Haberfehlner and coworkers extended the capabilities of conventional electron tomography to 3D localized elemental analysis by extracting the signals from the energy-dispersive X-ray (EDX) spectroscopy, low-loss and core-loss EELS at each voxel in 3D<sup>70</sup>. Goris and coworkers have performed the reconstruction on the raw EELS data and the reconstructed spectra can spatially resolve the valence states of Cerium ions in its oxide compound<sup>79</sup>.

In thesis, the spectrum-imaging (SI) dataset in EFTEM imaging mode was acquired as basis for tomographic reconstruction. One of technical novelties developed in this thesis is the fitting of the reference plasmon peaks of Si, amorphous SiC (a-SiC) and crystalline SiC in 3C-SiC phase into the low-loss region in EELS. The acquisition of the EFTEM SI dataset and the fitting results of plasmon peaks into the low-loss region are described in **Chapter 2.2**. Compared with BFTEM images, the improvement of contrasts in extracted plasmon images from the fitting modes is clearly visible. Additionally, the other technical novelty is the development of 4D electron tomography based on the raw EFTEM SI dataset in the low-loss region which is discussed in **Chapter 4.3**. It is important to point out that no filtering, noise reduction, or any other data processing was applied on the raw EFTEM SI dataset before and after the tomographic reconstruction. Currently, the raw dataset is still under the evaluation using advanced statistic treatments and the results presented in **Chapter 4.3** are the first preliminary results.

## 2. Synthesis and analysis of PV absorber layer

The advantages of using NPs based absorber layer for third generation solar cell are obvious. Several nanotechnology approaches have been proposed to improve the efficiency of NPs based solar cells<sup>83,84</sup>. The tunable band gap depending on the NPs size enables the NPs based absorber layer to increase the light harvest in the sunlight spectrum. Due to this quantum confinement effect, the semiconductor NPs based solar cells were demonstrated as having higher solar energy conversion efficiency than the traditional p-n junction silicon crystalline solar cells<sup>85</sup>. Si is the second most abundant element on earth and it is non-toxic and cheap, therefore, the fabrication of Si NPs embedded within semiconductor host matrices has been proposed as an excellent absorber layer that can be integrated into the third generation solar cells<sup>11</sup>. In **Paper V**, new synthesis methods were developed to fabricate Si NPs or Ge NPs based nanocomposites that can be used as absorber layers in third generation solar cells (**Chapter 2.1**). Since the dimension of NPs and interfacial nanostructures is in nanometer-scale, TEM becomes the only tool capable of directly measuring the size and morphology of NPs and nanostructures. The sample preparation for TEM analysis is discussed in **Chapter 2.2.1**. Since the structure and the chemical composition of the synthesized nanocomposites differ from each other (**Table 3**), different TEM analysis techniques had to be used for the samples from the different synthesis techniques. The choice of technique is discussed in **Chapter 2.2.2**. Ion beam analysis in **Chapter 2.3.1** was chosen as a additional characterization technique to inspect the impurities in the deposited film and analyze the chemical composition in the high temperature annealed SRSC films. Raman spectroscopy in **Chapter 2.3.2** was used to measure the crystallinity of Si NPs in the high temperature annealed SRSC films.

### 2.1. The deposition of the absorber layers

New synthesis methods, including chemical vapor deposition (CVD), physical vapor deposition (PVD) and aerosol-assisted CVD (AACVD), were developed for fabricating Si NPs based absorber layers for third generation solar cells. Using much lower processing temperature than the traditional high temperature annealing process was addressed in new synthesis methods. This is particular interesting for PV applications with temperature sensitive glass or polymeric substrates. In addition to the advantage of low processing temperature, new methods are capable to produce NPs with a desirable 3D density using the SiC (**Paper IV**) or transparent conductive oxides (**Paper I**) as host matrices. The synthesis of NPs was optimized in terms of size and density which was characterized by using TEM. Thereby, TEM analysis provides valuable information that helps the synthesis optimization to achieve the accurate control on the nanostructures. In this thesis, four syn-

thesis strategies including wet chemical process, PVD process, CVD process and high temperature annealing process were adopted by the collaborating groups to produce Si NPs embedded in the semiconducting host matrices, such as SiC, zinc oxide (ZnO) and indium tin oxide (ITO).

The commonly used methodology to fabricate the Si NPs embedded in a matrix material is based on the deposition of either single or multilayer of Si rich nanocomposite in which the excess Si precipitated from the surrounding matrix and form NPs through the high temperature annealing process, usually above 1000 °C <sup>11,17,39,86</sup>. In this thesis, this method is called as high temperature annealing process. Thin hydrogenated amorphous SRSC films were deposited by using the PECVD method. For the deposition, a mixture of silane and methane gases was used. The films were deposited on 1 mm thick fused quartz substrates kept at 360 °C. The annealing was performed in a crucible mounted in a heating stage. During the annealing the heating stage was purged with nitrogen with a flow of 60 ml/min. The gas purity was 99.997 % and the measured oxygen content was 0.3 ppm. The samples were annealed for different times (15 and 60 minutes) at 1100 °C. In the high temperature annealing process, a deeper understanding on the formation of the precipitated nanostructures and interfacial nanostructures was developed in **Paper VII**. However, it is still difficult to fully control the distribution of the precipitated c-Si NPs. The deposition of SRSC films and annealing normally requires high vacuum condition and clean room facilitates, thus the alternative methods for Si NPs synthesis are highly desirable.

Direct nucleation of Si NPs by a CVD process is a promising method to synthesize Si NPs with lower substrate temperature compared to the high temperature annealing process described above. Baron et al. have reported the possibility to fabricate the Si NPs onto insulating substrates by controlling the early stage of the Si on a CVD reactor <sup>87</sup>. Amorphous SiC thin films were deposited by PECVD on Si substrates kept at 200°C during the deposition. Then, samples were transferred to a low-pressure CVD (LPCVD) reactor. In LPCVD reactor, the nucleation and growth of Si NPs onto the a-SiC surface was carried out by thermal decomposition of silane in hydrogen at 700°C under a pressure of 20 Torr for 20 seconds to 35 seconds. The structural information of the a-SiC layer and c-Si NPs need to be analyzed by TEM. More details on this part of the study and a thorough analysis of the results are given in **Paper IV**.

Compared with the high temperature annealing and CVD processes, one alternative way to grow Si NPs is by condensation of a Si vapor which was sputtered by ionized argon in a dedicated magnetron-based PVD reactor <sup>88</sup>. The detailed description of PVD reactor chamber and deposition parameters can be found in [88]. In the PVD process, the size distribution of NPs can be



well controlled in nanometer-scale using different materials, such as metals or semiconductors. The special feature of this PVD process is that the crystallization of NPs takes place in the inert-gas phase of the sputtered nanoparticle source before reaching the substrate. During the whole process, no heating of the substrate is required. Two materials systems deposited by PVD were studied, Si NPs in aluminum doped ZnO (ZnO:Al) matrix (**Paper V**) and Ge NPs in ZnO:Al matrix (**Paper III**).

Compared with the dry processes described above, using the wet chemical process to fabricate NPs has been attracting increasing attention recently<sup>89</sup>. In the wet chemical process, NPs can be synthesized and deposited onto a large-area of the substrate at much lower temperature with relatively low cost, comparing to the dry processes described above. The synthesis of Si NPs was adapted the reported method by Tilley and coworkers<sup>89</sup>. Indium tin oxide (ITO) was chosen as a matrix material for Si NPs. Si NPs based nanocomposite was synthesized from a precursor solution consisting of a 5:1 ratio of Si NPs : ITO (neodecanoate) deposited onto the Si substrate at 450°C using the AACVD technique. The deposited films were annealed at 300 °C in the forming gas in order to reduce the resistivity of the ITO matrix<sup>90</sup>. The detailed information on the chemicals and solutions used for the nanocomposite synthesis can be found in **Paper I**.

All the absorber layers were synthesized by collaborating groups in Europe. The structural and chemical properties of synthesized Si NPs based absorber by different methods vary from each other. TEM has been used as a powerful tool to characterize the structural and chemical properties of synthesized Si NPs based absorbers using different techniques.

## 2.2. Transmission Electron Microscopy

In this thesis, the TEM has been applied as a major analysis tool for characterizing the materials. The modern TEM is capable to analyse samples by a number of different imaging and spectroscopic signals such as: imaging down to the atomic level, structural information from electron diffraction, chemical analysis using electron energy-loss spectroscopy (EELS) or energy dispersive X-ray spectroscopy (EDS), electron magnetic circular dichroism (EMCD) to measure the magnetic properties, electron holography and electron tomography. The standard TEM techniques in 2D characterization used in this thesis are briefly discussed in this chapter, and more complete descriptions can be found in the text books, from Williams<sup>91</sup> and Egerton<sup>92</sup>. In this thesis, all the TEM experimental results were obtained from a FEI Tecnai F30-ST TEM operated at 300 keV (**Figure 3**). The microscope is equipped with a field emission gun (FEG), a post column spectrometer (Gatan GIF 2002 spectrometer until 2013 which was replaced by a Gatan Tridiem

spectrometer in 2013 until now) and an EDS system. For the development of electron tomography, all the tilt series were acquired manually using a Fischione model 2020 tomography sample holder which enables a double tilting experiment.

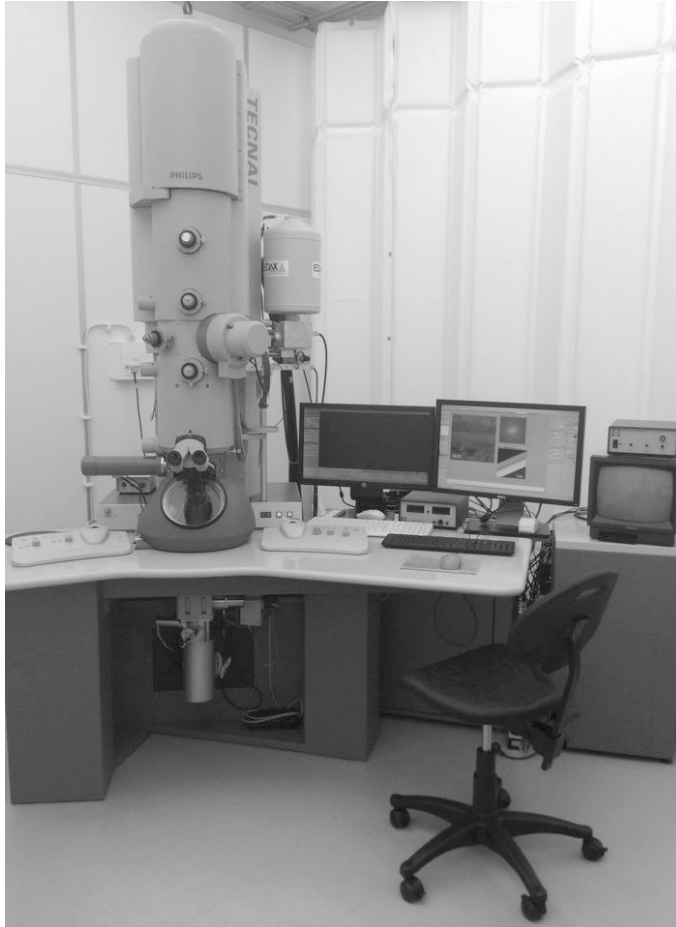


*Figure 3: Photo of the FEI Tecnai F30-ST 300 keV FEG instrument, situated at the Ångström laboratory, used in this thesis. The microscope is now equipped with a Gatan Tridiem spectrometer.*

In TEM, fast electrons transmitted through a thin specimen are collected and analyzed. From the top down, the TEM consists of an emission source, which is a filament or a tip (a tungsten filament or a lanthanum hexaboride filament), connected to a high voltage source (typically 100 ~ 300 kV). In a field emission gun (FEG), an applied extraction voltage enables the filaments to emit electrons by electric field extraction into the vacuum. The emitted electrons can be focused onto the specimen with the desired size and

dose using a series of lenses and apertures above the specimen. A TEM specimen must be thin enough for the electrons to be transmitted through (typically less than 100 nm), the transmitted electrons carry the important information from the specimen and need to be further directed by a set of lenses and apertures below the specimen. The detailed sample preparation was discussed in **Chapter 2.2.1**. Similar to the optical glass lenses, the objective lenses below the specimen used in the TEM help form a back focal plane and image plane. The electron diffraction patterns containing structural information of the specimen appears in the back focal plane. When forming images of the specimen in TEM, the contrasts in the image are strongly depending on the selection of the transmitted electrons.

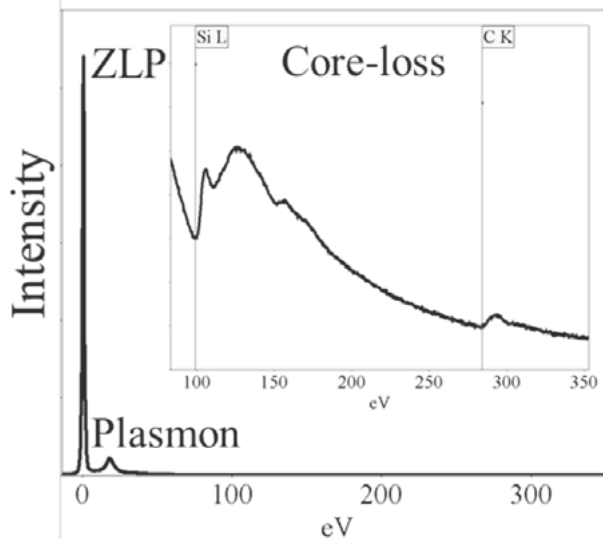


*Figure 4: A typical EELS spectrum showing the characteristic peaks such as ZLP, plasmon peak. The inset EELS spectrum shows the core-loss peak of Si L<sub>2,3</sub> edge with an onset at 99 eV and C K edge with an onset at 284 eV. The overview and core-loss EELS spectra were acquired separately from the high temperature annealed SRSC film.*

The incident electrons in the TEM can be scattered inelastically, energy is then transferred from the incident electrons to the sample, for example, ionizing an atom by exciting a core electron. The transferred energy (called as electron energy loss) is characteristic and depends on the elemental composition of the materials. The electron energy losses of the inelastically scattered electrons can be measured by a post-column electron energy loss spectrometer. The magnetic prism in the spectrometer can be used to separate the electrons with different energy losses, thereby the distribution of electrons with different energy losses can be recorded as an EELS spectra on a charge cou-

pled device (CCD) camera. A typical EELS spectrum was shown in **Figure 4**.

From the recorded energy-loss spectrum (**Figure 4**), one can easily see the features, such as the zero-loss peak (ZLP) which is the distribution of electrons with no energy loss, plasmon peaks which were attributed by the electrons inelastically scattered with the weakly bound electrons in outermost atomic orbitals and inner-shell ionizations with fine structures in atoms. The ZLP is normally the most intense peak compared with all other featured peaks in EELS. The full width at half maximum (FWHM) of the zero-loss peak defines the energy spread of the incident electrons (typically 0.1 eV to 2 eV for the modern TEM). The plasmon excitation dominates in the region of 7 eV to 50 eV (also called as low-loss region). Plasmons can be imagined as joint oscillations of weakly bound valence electrons<sup>93</sup>. For the inner-shell ionization (also called as core losses), depending on which transition is excited, the core-loss energy is denoted according to the Bohr shell. For example,  $L_{2,3}$  corresponds to  $2p_{1/2,3/2}$  electrons excited to 3d and 4s states. The onset of Si- $L_{2,3}$  edge is at 99 eV (as shown in **Figure 4**). The TEM can not only record EELS spectra but also acquire EFTEM images or energy filtered diffraction patterns by using the energy slit. By placing the energy slit on the specific electron energy loss, EFTEM imaging is an excellent tool for chemical analysis. EFTEM imaging using the three-window-method has been demonstrated as a powerful technique to generate elemental mapping<sup>94</sup>.

In this thesis, a more advanced chemical analysis method called EFTEM SI technique was applied. In EFTEM SI, a small energy slit (2eV energy slit) was chosen and a series of energy filtered images are acquired with a small continuous offset in energy ( $\Delta E \approx 1\text{eV}$ ). In this way a 3D dataset (illustrated in **Figure 5**) consisting of the energy filtered images in XY plane and electron energy loss along the Z direction is obtained<sup>95</sup>. The EELS spectrum can be reconstructed at every column of pixels in the energy filtered images. This way to create such a 3D dataset called as EFTEM-SI dataset, containing the chemical information with a high spatial resolution. The energy resolution was determined by the size of the energy slit and the spatial resolution was mainly influenced by the chromatic aberration and experimental settings of TEM. It is possible to obtain the filtered image with a spatial resolution down to sub-nanometer range<sup>96</sup>. The technical details about the SI technique in EFTEM or STEM modes and related data processing can be found in the literature<sup>93,97</sup>.

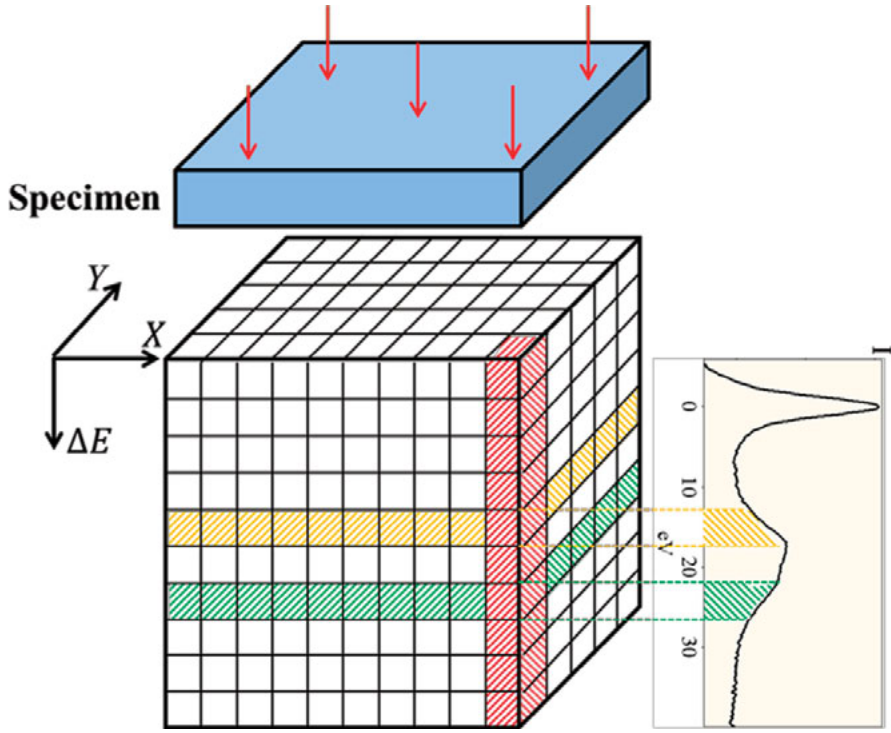


Figure 5: The scheme shows the formation of an EFTEM SI dataset. In the  $XY$  plane, the energy filtered images are formed, and EELS spectrum is constructed along the  $\Delta E$  direction.

Such a SI dataset can be carried out in both scanning and conventional TEM, the relative advantages and pitfalls of EELS acquisition in these two modes have been already extensively discussed<sup>98</sup>. Before starting the SI acquisition, several factors need to be carefully considered, such as the number of pixels in the region of interests, the choosing of the EELS signal, the beam current, the acquisition time and the sample stability. In STEM mode, an energy loss spectrum is acquired at each of a succession of scanned pixels along the  $Z$  direction, thus a 3D dataset is created. In this thesis work, when STEM-EELS SI was applied on the annealed SRSC films, the charging effect plays a role and causes the sample to drift significantly during the data acquisition. One of successful STEM-EELS SI datasets was acquired on a very thin ( $\sim 8$  nm) and small ( $20 \text{ nm} \times 20 \text{ nm}$ ) area, no substrate quartz was included in this region, thus the charging effect was minimized. The STEM-EELS SI result was used in **Chapter 4.3** to characterize the relative compositional change of Si to Carbon (C) after the spinodal decomposition process, using the core-loss EELS signal of Si L-edge and C K-edge. For the tomography data acquisition, STEM-EELS SI was not chosen because a larger area ( $300 \text{ nm} \times 300 \text{ nm}$ ) is needed for the convenience of the image stack

alignment, and then the charging effect from the quartz substrate plays a role during the scanning.

### 2.2.1. Sample preparation for TEM

The sample preparation is the first step that needs to be well planned before the TEM analysis. The key principle is that the sample preparation does not change the properties of the sample that we are going to analyze using TEM. In this thesis, the classical TEM sample preparation techniques including dimple grinding and ion milling have been used<sup>99</sup>. For the cross sectional sample preparation, the sample materials were first cut into small pieces and two of the small pieces of sample materials were picked up and clamped into a Ti grid (brought from the Technoorg Linda, [www.technoorg.hu](http://www.technoorg.hu)). Then, the grid and sample materials were fixed by epoxy glue and rough and fine polished from the both sides to obtain a sample of a thickness of approximately  $80 \sim 90 \mu\text{m}$ . After the polishing, dimple grinding was performed on the both sides of the Ti grid using Gatan dimple grinder model 656. The dimple grinded samples should have a thickness of about  $10 \mu\text{m}$ . After the dimple grinding, the samples were ion milled using a Gatan Precision Ion Polishing System (PIPS, Ar-ions) model 691 to be electron transparency. For the plan view sample preparation, a Gatan ultrasonic disc cutter model 601 was used to cut the sample into 3 mm discs. Then, the samples were polished, dimple grinded and ion milled on the substrate side of the samples. The most critical step during the sample preparation is the ion milling, the whole milling process can be divided into two steps: (i) the incident angle was set to be  $6^\circ$  with an acceleration voltage of 5 keV on Ar ions; (ii) when the red transmitted light (only applied on the Si substrate) starts appearing<sup>100</sup>, then the incident angle was set to  $4^\circ \sim 5^\circ$  with a lower acceleration voltage of 2.5 keV. The total amount of time spent on the ion milling depends on the thickness of the sample after dimple grinding. Normally, if the sample thickness is about  $10 \mu\text{m}$  after dimple grinding and using the above recipe of ion milling, it takes about 30 ~ 40 minutes of ion milling to make the sample electron transparent. A plan view sample prepared using above recipe is shown in **Figure 6**.

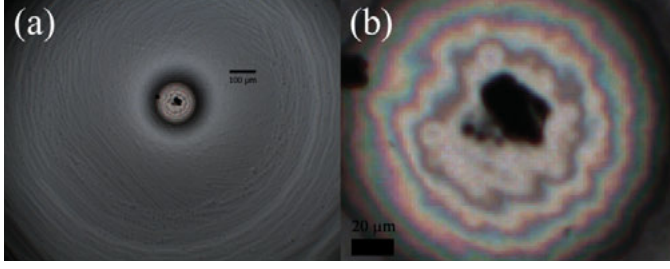


Figure 6: (a) Optical image (top illuminated) on a TEM sample prepared in plan view geometry. (b) the interference pattern of the light with a hole in the center.

Normally, after the ion milling, the sample materials have a wedge shape in the thinnest region and from the interference pattern appearing in the optical microscopy images, the thickness of the sample in the thin regions can be estimated<sup>101</sup>. The dark minima appear when  $2nt = m\lambda$ ; thus,  $t_1 = \lambda/2n$ ,  $t_2 = \lambda/n$ ,  $t_3 = 3\lambda/2n$ , and so on<sup>101</sup>. Where  $n$  is the refractive index of Si,  $\lambda$  is the wavelength of the light. We can take the wavelength of 550 nm, near the center of the visible spectrum and Si refractive index of 3.44<sup>102</sup>. The thickness at  $t_1 = 80 \text{ nm}$ ,  $t_2 = 160 \text{ nm}$ ,  $t_3 = 240 \text{ nm}$ , which means that the whole region from the hole (appears as dark contrast in **Figure 6**) to the first fringe  $t_1$  has a thickness less than 80 nm with a diameter about 40  $\mu\text{m}$ .

Electron tomography technique using the BFTEM images was applied to examine the sample morphology at the thinnest region as shown in **Figure 7**. From the (a) to (e), one can see the sample thickness is about 5 nm -10 nm. From the 3D view in (f), the curvature of the sample was clearly shown near to the edge which was considered as the retarding region of the low energy ions (0 ~ 2.5 keV)<sup>99</sup>. Moreover, the change of the film thickness in red marked regions can be observed from the (a) to (e), this indicates the roughness of the prepared film which is less than 1 nm. The dark dot like contrasts seen in **Figure 7** (a) to (e) are NPs which are presented as green particles in the 3D view **Figure 7** (f). For all the TEM samples, they were analyzed directly after the ion milling in order to minimize the oxidation effect. For further details in a particular case, see description in the respective article.

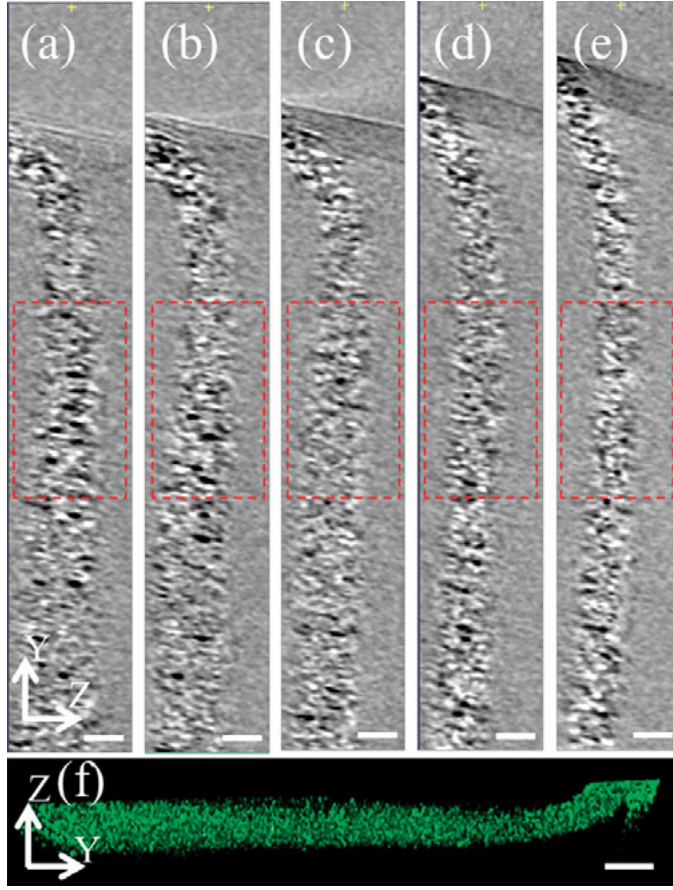


Figure 7: (a)-(e) five slices extracted in the YZ planes from the reconstructed tomogram. (f) 3D view of a plan view sample segmented by isosurface method. The scale bars are 5 nm.

### 2.2.2. Contrast optimization of NPs in the investigated samples

The different synthesis strategies adopted to fabricate NP based absorber layers result in differences in structural and chemical properties of NPs. The different synthesis strategies involve many technological steps, a small change in processing parameters in one step could bring a significant structural modification in nanometer scale. Therefore, TEM was applied to characterize the structural and chemical properties of NPs based absorber layers with a very high precision and accuracy. For each synthesized absorber layer different and specific TEM analysis goals needed to be achieved (**Table 3**).



Synthesis conditions	Film architectures	Goals of the TEM analysis
<b><i>Wet chemical process</i></b>		
For synthesis of Si NPs, the reported method by Tilley et al. was adapted <sup>89</sup> . Si NPs based nanocomposite films prepared from mixture of 1:5 ratio of ITO/Si NPs using the AACVD method <sup>103</sup> . Deposited films annealed at 300 °C in forming gas.	Si NPs were embedded in the ITO matrix, the whole film was deposited on the Si substrate.	<ol style="list-style-type: none"> <li>1. To analyze if the Si NPs were oxidized by the host matrix after the annealing.</li> <li>2. 3D distribution and density of Si NPs.</li> </ol> <b>(Paper I)</b>
<b><i>Physical vapor deposition process</i></b>		
The synthesis of Ge NPs was achieved by condensation of an atomic vapour produced by magnetron sputtering of a Ge target <sup>88,104,105</sup> . The Ge NPs were covered by a ZnO:Al thin film by using the ion beam sputtering (IBS) setup in the same magnetron sputtering chamber <sup>88,104,105</sup> .	A layer of Ge NPs was deposited on the Si substrate and covered by a ZnO:Al layer that construct a p-i-n junction configuration.	<p>To confirm the p-i-n junction configuration by analyzing if the ZnO:Al layer penetrates into the Ge NPs stacking layer in the cross sectional geometry.</p> <b>(Paper III)</b>
<b><i>Chemical vapor deposition process</i></b>		
The amorphous SRSC layer was deposited on the Si substrate using the PECVD method. The Si NPs were grown on top of the amorphous SRSC layer using the LPCVD method at 700 °C.	Si NPs were grown on the amorphous Si rich SiC layer which was deposited on the Si substrate.	<ol style="list-style-type: none"> <li>1. To analyze if the crystalline Si NPs are formed in the SRSC layer during the annealing at 700 °C for 20 seconds.</li> <li>2. Size distribution of Si NPs.</li> </ol> <b>(Paper IV)</b>
<b><i>High Temperature annealing process</i></b>		
The amorphous SRSC films were deposited on the quartz substrate using PECVD method. In order to crystalize the excess Si, the films were annealed at 1100 °C for 1 hour. The similar method was reported by Kuenle and coworkers <sup>38,39</sup> .	Si NPs were crystalized during the annealing process and embedded in the SiC matrix. The whole SRSC films were deposited on the quartz substrate.	<ol style="list-style-type: none"> <li>1. Identify the precipitated NPs.</li> <li>2. Study the 3D morphology of the precipitated NPs.</li> <li>3. Study the interfacial nanostructures between the precipitated NPs.</li> </ol> <b>(Paper II and VII)</b>

*Table 3. The synthesis strategies of the NP based absorber layers for third generation solar cells and the goals of the TEM analysis.*

Bright field TEM (BFTEM) imaging together with the selected area diffraction (SAD) patterns can contribute knowledge about the size distribution of crystalline NPs (**Paper I, II and IV**) and the crystalline phase of NPs (**Paper I and IV**). When two different crystalline phases of NPs are coexisting, it is useful to identify the crystalline phases (**Paper VII**) from SAD patterns. High resolution TEM (HRTEM) images can locally identify the crystalline phase of NPs by indexing the reflection spots in the Fourier transform of the HRTEM image (**Paper V**). The application of BFTEM, HRTEM images and SAD patterns has proven to be an excellence combination to characterize the size and structural properties of crystalline Si NPs and meet the analysis goals listed in **Table 3** for the wet synthesis process (**Paper I**) and the CVD process (**Paper IV**) NPs.

For the high temperature annealing process and PVD process, conventional BFTEM and HRTEM imaging is insufficient to answer the questions related to the NPs properties, because of the coexistence of two different crystalline NPs in both cases. In the high temperature annealed SRSC film, both c-Si and 3C-SiC NPs were observed from the reported SAD patterns<sup>37–39</sup>. It is difficult to identify these two types of crystalline NPs from the BFTEM images. Similar to the NPs synthesized by PVD process, from BFTEM and HRTEM imaging we were not able clearly identify crystalline phases of ZnO and Ge NPs. Moreover, BFTEM and HRTEM imaging are mainly sensitive to those crystalline NPs which are well oriented to the electron beam. Thereby, a certain amount of crystalline NPs was not detectable and nanostructures in amorphous phase were not clearly observable in BFTEM and HRTEM images. Therefore, a technique on TEM to obtain images in which the contrast directly reflects the chemical composition of NPs is desired.

In **Paper III**, in order to better control the p-i-n junction, EFTEM imaging using the three-window-method has been applied to analyses the penetration of the ZnO:Al layer into the Ge NPs layer which was deposited by PVD process. In BFTEM images, both the layers of Ge NPs and ZnO NPs appear as dark contrasts due to the high crystallinity of NPs and the penetration of ZnO:Al layer can not be determined. To acquire EFTEM images, a 20 eV energy slit was selected to generate the background under the core loss edges from two energy filtered images in the pre-edge region of Zn L-edge, and one image on the Zn L-edge. Then, the extrapolated background image was calculated from two pre-edge energy filtered images and subtracted from the image taken at a post Zn-L edge energy. This results in a new image which corresponds to the elemental map of Zn. In the EFTEM image, the strong penetration of ZnO:Al layer into Ge NPs layer was clearly visible when the density of Ge NPs is relatively low. In this technique, the power-law background modeling only fits well when the sample is relatively thin ( $t/\lambda < 1$ )

and for energy losses higher than 200 eV<sup>94</sup>. The thickness of the sample region chosen for EFTEM elemental mapping in **Paper III** is  $t/\lambda \approx 0.4$ .

EFTEM using the low-loss signal in EELS spectra has been applied as a powerful technique for the purpose of identifying the chemical information of precipitated Si NPs from the SRSO or SRSC films<sup>13,16,17,38,39,106</sup>. The plasmon energies of c-Si, a-Si, SiO<sub>2</sub>, amorphous SiC (a-SiC) and 3C-SiC are located at 16.4 eV<sup>93</sup>, 16.7 eV<sup>93</sup>, 23 eV<sup>93</sup>, 20 eV<sup>38</sup> and 22.5 eV<sup>38,39</sup>, respectively. The plasmon energies in a range of 10 eV~12 eV can be the surface plasmon<sup>93</sup>. In the case of high temperature annealed SRSC films, the low-loss region in EELS can be considered as a mixture of individual volume plasmon peak of Si, a-SiC, 3C-SiC and Si surface plasmon.

To image the Si NPs embedded in SiO<sub>2</sub> matrix, 4 eV energy slits were set on the energy dispersive plane to select electrons with 17 eV Si plasmon energy loss. Then, an energy filtered Si plasmon image can be obtained after the reconstruction of the image by the lenses of the GIF. The image is then recorded on the CCD camera. In this way, the whole population of Si NPs or Si nanostructures can be seen in the energy filtered Si plasmon image. The EFTEM imaging using a single energy slit on Si plasmon energy has been used as a method to optimize the contrasts of Si NPs or Si nanostructures embedded in SiO<sub>2</sub> or SiC matrix<sup>13,16-18,38,39,106</sup>.

Since the FWHM of SiO<sub>2</sub> plasmon peak can be higher than 15 eV<sup>93</sup>, there must be SiO<sub>2</sub> plasmon signal included in Si plasmon images by using a 4 eV energy slit placed on the 17 eV. To solve this problem and improve the signal to noise ratio (SNR) in Si plasmon images, a reference spectrum of Si plasmon peak was proposed to be fitted to the plasmon peak acquired in the STEM-EELS SI mode. From this fit, we obtain the weight of Si at one place in the image, and from fitting the spectra at every image pixel, a Si plasmon image can be extracted, where the weight of the Si plasmon peak at one pixel corresponds to the grey level intensity in such Si plasmon images. Such maps generated from fitted plasmon spectra are more representative for Si phase (or to a minor extent of the SiO<sub>2</sub> phase) than images obtained from a single window close to the Si plasmon peak since the overlap between the Si and the SiC plasmon can not be well controlled in this latter technique<sup>106</sup>. Therefore, the extraction of Si phase by fitting the reference spectrum into the SI dataset is more advanced way to optimize the contrast in Si plasmon images.

The existing structural analysis on the high temperature annealed SRSC films was limited by 2D BFTEM, HRTEM, EFTEM images and SAD patterns<sup>36-39</sup>. In this thesis, for the first time, the EFTEM SI technique was applied to analyze the detailed nanostructures formed in annealed SRSC film. The sample thickness for acquisition of EFTEM SI dataset is about 20

nm. EFTEM SI datasets were acquired from -4 eV to 40 eV with 2 eV energy slit and 1 eV as energy steps using a 7.6 mrad semi collection angle. The spectrometer installed in the used TEM corrects up to second order aberrations and enables the use of the energy slits equal to or above 2 eV in size. The ZLP was used to calibrate the energy shift. The offline spectrum treatment includes Fourier log deconvolution to remove the plural scattering<sup>107</sup>, linear background subtraction, non-negative least squares (NNLS) fitting<sup>108</sup> on the plasmon region and extraction of plasmon images were performed using the DigitalMicrograph<sup>®</sup> program (www.gatan.com, Version: 2.30.542.0). The linear background under the plasmon peak results most likely from the surface plasmons and Cherenkov losses. This background model is interpolated between 5 eV and 35 eV. The whole plasmon region was fitted by four plasmon peaks, which are Si surface plasmon peak, Si plasmon peak, a-SiC plasmon and 3C-SiC plasmon peak shown in **Figure 8**. The center of the plasmon peaks of Si<sup>13,38,39,93,106</sup>, a-SiC<sup>38</sup> and 3C-SiC<sup>38,39,93</sup> were determined from the reported values. The FWHMs of the plasmon peaks are not constrained during the fitting and were determined by finding the minimum fitting residue. The size dependent plasmon energy shift<sup>109</sup> was also taken into consideration when the center of Si plasmon energy was determined. Since from the HRTEM images and reconstructed tomograms, the average size of Si NPs is above 5 nm (HRTEM images can be found in the supplementary figure 3 of **Paper VII**), thus it is reasonable to fix the center of Si plasmon peak in a range of 17 eV to 17.5 eV during the fitting tests. When the center of Si plasmon peak is fixed in this range, the a-SiC plasmon must be added in order to reduce the fitting residue at 20 eV. Thus, the fitting helps to confirm the existence of a-SiC plasmon peak at 20 eV. The detailed discussion on the fitting procedures to find the FWHM of each plasmon peak was presented in the supplementary information in **Paper VII**.

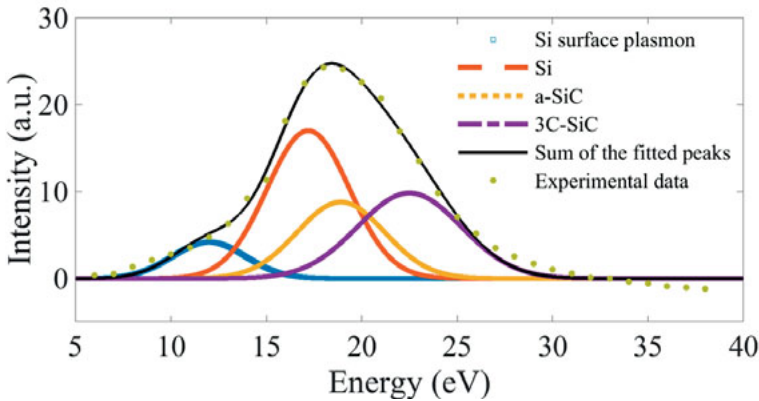


*Figure 8: The background subtracted EELS spectrum in the low-loss region. The whole low-loss region was fitted by four plasmon peaks represented by Gaussians.*

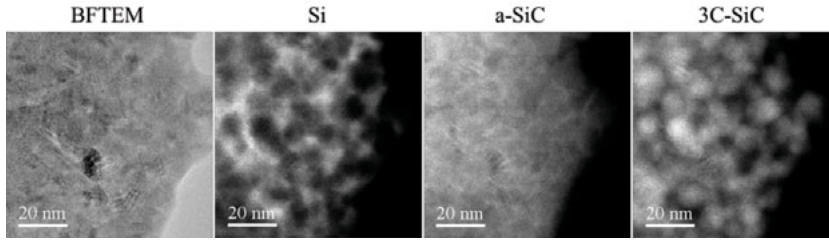


*Figure 9: The comparison between the BFTEM image and the plasmon images extracted at Si, a-SiC and 3C-SiC plasmon energies. Both images were acquired from 1 hour annealed SRSC film.*

The extracted Si, a-SiC and 3C-SiC plasmon images by using the fitting models are shown in **Figure 9**. The pixel value presented in the extracted plasmon images corresponds to the area of fitted plasmon peaks. The Si phase appears as a network like structure, while from the 3C-SiC plasmon image, the clear NPs like contrasts were observed. In the network like structure, some areas presented a triangular shape and these triangular areas seem to be connected by a filament like structure in 2D Si plasmon image in **Figure 9**. The triangular areas shown in the Si plasmon image were surrounded by 3C-SiC NPs, and are called as triple junction areas from now on. In particular, the a-SiC phase seems to be presented as a thin interface between the Si and 3C-SiC phases in 2D plasmon images. Both of these interesting observations obtained by analyzing the plasmon images can not be equally observed from the BFTEM image. The comparison of the contrasts between different imaging conditions in **Figure 9** underlined the strength of the EFTEM SI technique. Fitting the whole plasmon region with more than one plasmon peak and extracting the fitted plasmon images from the EFTEM SI dataset is the main result on the 2D contrasts optimization in this chapter. To confirm the 3D morphologies of the Si network structure and 3C-SiC NPs as well as the distribution of a-SiC as an interface, electron tomography technique was applied by using the 2D plasmon images (**Chapter 4**).

## 2.3. Additional characterization techniques

### 2.3.1. Ion beam analysis

Elastic recoil detection analysis (ERDA) was applied to accurately determine the chemical composition of the SRSC films analyzed in the **Paper VII**. A high energy ion beam is directed to a sample to be analyzed, and similar to the Rutherford backscattering (RBS) technique, there is elastic nuclear interactions between the incident ions and the atoms in the target sample. However, the differences between are ERDA and RBS are: (i) ERDA collects recoiled target atoms in the forward direction under a scheme of the time-of-flight detection, while the RBS collects backscattered ions; (ii) the ions

source used in ERDA are much heavier than RBS, thus, ERDA is much more sensitive to light elements (such as O, N, C). In this thesis, ERDA analysis was performed using Iodine (I) as the ion source with beam energy of 36 MeV, and the composition of SRSC film after 1 hour annealing is  $\text{Si}_{0.67\pm0.02}\text{C}_{0.33\pm0.02}\%$ . There is also oxygen ( $\sim 8\%$ ) detected in the annealed films from the ERDA analysis. This may be due to the fact that the SRSC films were kept in the air atmosphere for two months before the ERDA analysis.

### 2.3.2. Raman spectroscopy

Raman Spectroscopy was performed on a Renishaw in Via Raman microscope. A 514 nm excitation laser was used at 5% intensity. Measurements were performed at 100 second integration time and one accumulation. To understand the crystallization process of Si in SiC matrix, the analysis of the Raman peak corresponding to vibrations due to Si-Si bonds is particular of interest. Table 4 shows these bands and their origin.

Band origin	Band position ( $\text{cm}^{-1}$ )
Si-Si (amorph.)	Broad band centered around $\sim 480\text{ cm}^{-1}$
Si-Si (cryst.)	Sharp peak at $521\text{ cm}^{-1}$ and small hump at $920\text{ cm}^{-1}$ due to a two phonon mode.

Table 4: Band origins and their positions.

**Figure 10** shows the Raman spectra of sample  $\text{Si}_{0.6}\text{C}_{0.4}$  annealed for different times at  $1100\text{ }^{\circ}\text{C}$ . After 4 minutes annealing a crystalline peak starts to form and continues to grow with longer annealing times. The  $520\text{ cm}^{-1}$  as well as the  $480\text{ cm}^{-1}$  peak can shift due to structural changes in the material or measurement errors. The apparent peak shift at of the  $480\text{ cm}^{-1}$  peak was considered to be related to the increased crystallinity of Si during the annealing process<sup>110</sup>. By annealing, the amorphous Si peak does not disappear. Therefore, the analysis of Raman spectroscopy confirms that Si does not get completely crystallized after 1 hour annealing (**Paper V and VII**).

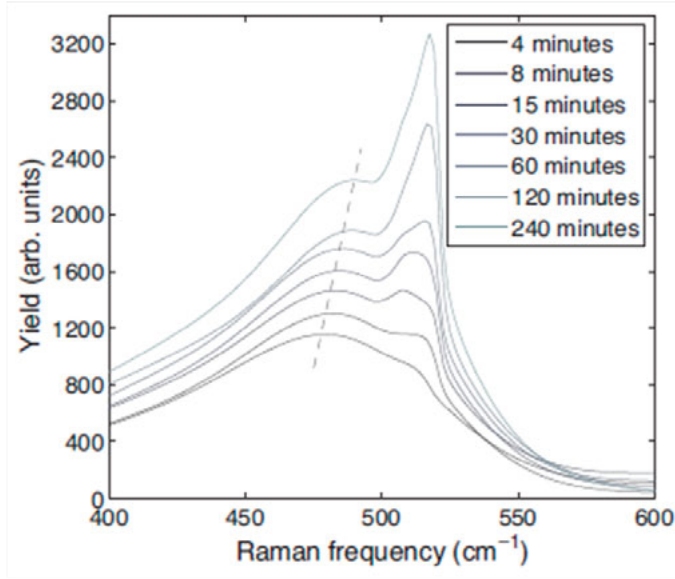


Figure 10: Raman Spectra of the annealed  $\text{Si}_{0.6}\text{C}_{0.4}$  films.

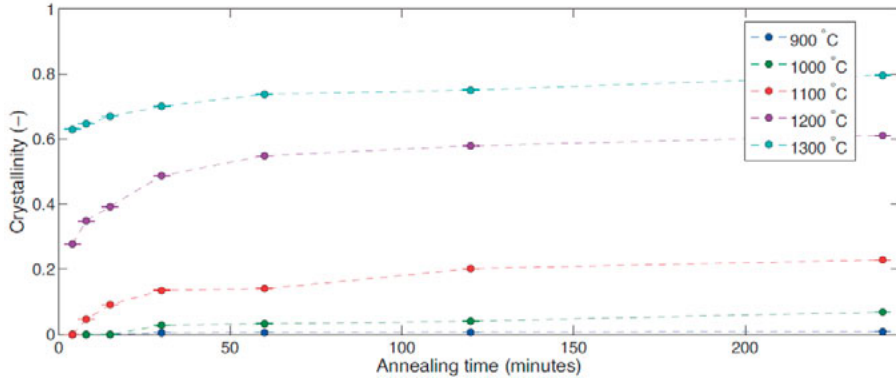


Figure 11: IRFR analysis on the crystallinity of Si in annealed  $\text{Si}_{0.7}\text{C}_{0.3}$  films at different temperatures as a function of annealing time.

It is important to obtain the crystalline fraction of Si for understanding the crystallization process of Si during the annealing. Based on the raw data of the Raman spectra of the annealed films, the crystallinity of Si can be carefully studied by using the Integrated Raman Fitting Routine (IRFR) shown in **Figure 11**. In this fitting routine, the phonon modes of the Si phase are represented by the longitudinal acoustic (LA), transverse acoustic (TA), longitudinal optical (LO) and transverse optical (TO) modes, and each mode was represented by Gaussian distribution. The phonon mode of the crystalline phase is represented by the phonon confinement model which is the TO mode of the crystalline Si phase<sup>111</sup>. The determination of the Si crystallinity

and the detailed discussion of IRFR method were reported by Smit and coworkers<sup>110</sup>.

In **Figure 11**, the main observations are: (i) after 1 hour annealing, the crystallinity of Si increases very slowly for a  $\text{Si}_{0.7}\text{C}_{0.3}$  film; (ii) the crystalline Si phase only takes about 15 at. % of the total amount of Si (amorphous phase plus crystalline phase) at 1 hour annealing; (iii) the crystallinity of Si is strongly temperature dependent. These observations confirm the existence of amorphous Si after the thermal annealing. Combined with the 3D analysis it can help us better understand the crystallization process of Si in SRSC films (**Chapter 4**).

## 2.4. Conclusion

Various characterization techniques were applied to study the absorber layers which have potential applications for the third generation solar cells. Among the techniques, TEM is the only tool that can directly measure the size of NPs, identify the chemical composition of NPs and characterize the nanostructures formed in the absorber layer with atomic resolution. In the analyzed cases, the size distribution of Si NPs synthesis by wet process and CVD methods has a more symmetric shape (**Paper I and IV**), while in the high temperature annealed SRSC film the size distribution of NPs becomes asymmetric and with a broadened width (**Paper II**). This suggests that the wet process and CVD process have better control to obtain more uniform size distribution of synthesized NPs than the high temperature annealing process. Depending on the contrast mechanisms on TEM, the contrast generated by the Si NPs or nanostructures in different imaging modes could lead to completely different interpretations, thereby the contrast optimization is an important step that can firstly improve the contrasts of Si nanostructures and secondly avoid the misunderstanding of the formation mechanism of Si nanostructures. On the other hand, the contrast optimization is a preparatory work for the electron tomography development which will be discussed in **Chapter 4**.



### 3. Electron tomography on TEM

Usually, the microscopic characterization of materials consists in projecting the structure of a sample into 2 dimensional XY plane. From this projection alone, it is not possible to retrieve the detailed structural information along the Z direction. However, nearly all microstructure of materials contains structural details varying in three dimensions. Precipitated NPs or protein aggregates are occupying certain volumes; interfaces between NPs and the crystalline lattices formed by protein granules are non-planar structures. Consequently, 2D characterization sometimes is not sufficient to reveal the real nature of a 3D object and can introduce errors or misunderstandings when the materials' structural properties were interpreted. Thus, a technique which can analyze microstructures in three dimensions with nanometer resolution is needed.

Electron tomography refers to an imaging technique which can produce the sections through the 3D object by reconstructing a series of 2D projections. This reconstruction of a series of 2D projections can be based on images coming from different signals acquired in the TEM. A detailed discussion of choices of possible signals for the development of electron tomography technique, the important technical information on alignment and reconstruction methods together with segmentation on 3D dataset is given in this chapter.

#### 3.1. The acquisition of the tilt series

There is a wide range of contrast mechanisms generated from TEM can be chosen as signals to acquire the tilt series. For the development of electron tomography, the contrasts in 2D images need to be monotonically varying with the properties of the samples along the straight lines through the sample. This is known as projection requirement for electron tomography on TEM<sup>112</sup>. The project requirement actually limits the number of TEM imaging techniques especially for crystalline samples. Diffraction contrast is dominate in imaging of crystalline samples and leads to non-monotonically varying contrasts depending on the orientations of crystalline samples with respect to the electron beam. Therefore, such contrasts, in general, do not fulfill the projection requirement. In general, the imaging techniques, which can be chosen for the development of electron tomography of crystalline samples, need to select and detect the incoherently scattered electrons such as HAADF STEM<sup>66,67</sup>, EELS<sup>68,69</sup> or EDS<sup>70,71</sup> mapping and EFTEM<sup>65</sup>.

The scattering events can also be distinguished between coherent and incoherent scattering depending on the change of electron wave vector before and after the scattering event. Elastic scattering is usually coherent, on the other hand, inelastic scattering is usually incoherent. Incoherent electrons are

always preferred for the development of electron tomography on crystalline materials because the contrast generated from incoherent electrons does not depend on the lattice orientation of crystalline materials, which is a prerequisite for electron tomography data acquisition. It means that BFTEM imaging in which the diffraction contrast dominates may not be suitable for crystalline sample in general. On the other hand, for most of the life science applications, BFTEM imaging can be used for the data acquisition, as the contrast depends on the type and density of life science samples during the interaction between the sample and electrons <sup>113</sup>.

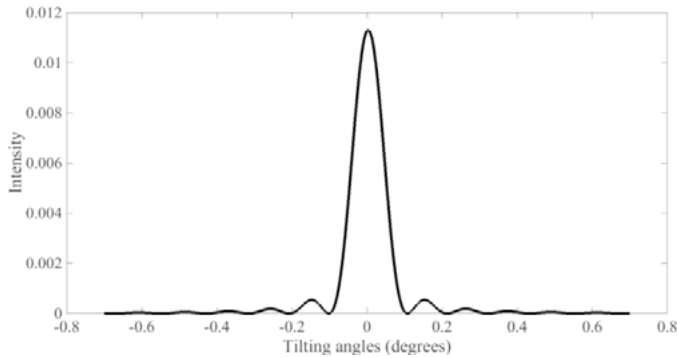


*Figure 12: The intensity of Si(111) diffracted beam calculated from the Howie-Whelan equations. The thickness,  $t=3$  nm and the extinction distance,  $\xi_{Si(111)}=88.41$  nm at 300 keV.*

In case of the crystalline materials, the incident electron beam is diffracted into a directly transmitted beam and diffracted beams. In general, the analysis of the diffracted beam intensity in TEM is not simple, because a diffracted beam can be easily re-diffracted, this repeated diffraction is called as “dynamical diffraction”. The Howie-Whelan equations then can be used to obtain the analytical expression for the intensity of the transmitted and diffracted electron beams as a function of specimen thickness  $t$  <sup>114</sup>. The calculation of the diffracted beam intensity as a function of tilting angles was performed by fixing the thickness of Si to 3 nm which is comparable with the size of the Si NPs measured from the TEM images (**Paper I and IV**). The calculated extinction distance can be found from the JEMs software <sup>115</sup>. In **Figure 12**, the intensity of the diffracted Si (111) beam takes about 1.2 % of the total beam intensity at the Bragg condition. Such a small contrast fluctuation during the tilting can influence the BFTEM tomography on small crystalline NPs. In our studied cases (**Chapter 4**), the contrast of NPs shown in BFTEM images through a tilt series does not change from 0 to 100%. The mass thickness contrast of NPs dominates in the BFTEM images and thus fulfills the projection requirement for electron tomography.

Other cases using diffraction contrasts to build up electron tomography technique should be mentioned as well. In the case of weak beam dark field (WBDF) imaging mode, the contrasts generated from dislocations still fulfil within a good approximation of the projection requirement necessary for tomographic reconstruction<sup>116</sup>. Later, it was shown that in the medium angle annular dark field (MAADF) STEM imaging mode using smaller collection angles than in the HAADF STEM imaging mode can produce even better reconstructions of dislocations using the beam precession electron diffraction to minimize the diffraction effect in high-resolution 3D imaging of dislocations<sup>117</sup>. However, these techniques were not treated in this thesis, because the EFTEM imaging using EELS signals shows superior contrasts than BFTEM imaging. Also, EFTEM imaging used here fulfils the projection requirement for the purpose of the tomographic reconstruction.

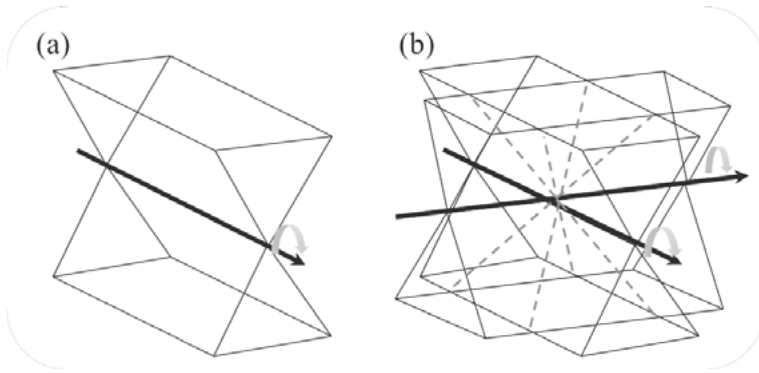


*Figure 13: Sampling of the Fourier domain by different acquisition geometries. (a) the missing wedge existing in the single tilt tomography, (b) the missing pyramid existing in the double tilt tomography which is marked by dashed blue lines.*

In materials science, a lot of efforts have been made in electron tomography to improve the resolution as well as explore new imaging techniques. Improvements in electron tomography have been achieved by optimizing acquisition methods and advanced reconstruction algorithms. Missing wedge artifacts is a major problem in electron tomography (**Figure 13**). For a full tomographic reconstruction, the tilt series should include images acquired in an angular range of  $\pm 90^\circ$ . In practice though, most tilt series contain images from an angular range of  $\pm 60^\circ$ - $70^\circ$ . This artifact leads to the decreased resolution along the Z direction and the elongation of sample features along the Z direction. Dual-axis tomography has been introduced reduce this artifact<sup>118</sup>. Another way is to have a needle shape sample prepared by FIB, instead of as a thin lamella, and then special sample holders have been pro-

duced to take the needle shape sample so that it allows the sample to be tilted over a full tilt range of  $180^\circ$ <sup>119</sup>.

New reconstruction algorithms have been proposed to improve the resolution. The first such technique is called discrete tomography<sup>120</sup>. In discrete tomography it is assumed that only a limited number of discrete grey levels exist in the reconstruction, in the simplest case only two levels and also by including prior knowledge about the sample, electron tomography in atomic resolution can be achieved in this way. Based on this technique, compressed-sensing based reconstruction and total variation minimization reconstruction has also been demonstrated to achieve atomic resolution<sup>121</sup>. In these techniques, the grey levels of the signals in reconstructed tomograms are assumed to be locally constant, and strong prior assumptions about the morphology of the object are made. In this thesis, a large number of NPs or nanostructures in a certain volume were targeted and the morphology of the targeted nanostructures is unknown, thereby the discrete tomography technique is not suitable for this work. To reduce the missing wedge artefact, the dual tilt series was utilized to improve the resolution in Z direction and the conventional back-projection reconstruction method was applied (discussed in **Chapter 3.3**).

### 3.2. Alignment

Alignment of the projections is a critical step in electron tomography. Due to the small size of samples, the stability of sample stages for TEMs is generally not sufficiently high to keep a common tilt axis in the center of all projections during the acquisition of a tilt series. Acquisition of a tilt series in a TEM generally requires re-centering of the sample before the acquisition of each projection, which is usually done by shifting the sample. While this allows keeping the region of interest inside the field of view, the projections are generally not aligned to each other after acquisition, i.e. there is no common line (tilt-axis) in the center of the projections around which sample features are rotating. Therefore before reconstruction electron tomography necessitates an alignment step.

Alignment is frequently split into two parts. In the first part, the shift alignment, the shift between the projections is calculated with the goal of finding alignment parameters, for which a common tilt-axis exists for all projections. The second step is the alignment of this tilt-axis, the position of the tilt-axis needs to be identified, its shift with respect to the center of the images and its angle with respect to the y-axis of the images.

For shift alignment the most commonly used techniques are alignment by cross correlation of subsequent tilt images<sup>122</sup> and marker-based align-

ment<sup>123</sup>. For cross-correlation methods, the cross-correlation between two subsequent images is calculated and the position of the maximum of the cross-correlation gives the shift between the images. Usually, before calculation of the cross-correlation, filters are applied to the 2D images to improve the contrast so that it helps the cross-correlation calculation, especially useful for the cryo-TEM tomography<sup>124</sup>.

An alignment method, which is used frequently in tomography for life science applications is the alignment based on markers. For this purpose, markers, usually gold beads, are deposited onto the both sides of the sample. In the alignment step the trajectories of these markers are recorded and based on center of mass calculations. Marker-based alignment methods also provide directly the alignment of the tilt axis, while the other methods in particular cross-correlation based methods do not.

There exist several possibilities to find the correct position of the tilt axis. The technique mostly used in this work is to use markerless alignment method<sup>125</sup> to align the image stacks. Because, adding new NPs for the purpose of alignment for the NPs contained samples can bring the difficulties in distinguishing the markers and targeted NPs. The markerless alignment method is to track the features through the image stacks so as to find the direction of the tilting axis. Either using markerless or marker based alignment methods, the ultimate goal is to adjust the alignment parameters to reduce the “banana-shaped” misalignment artifacts in the reconstructed tomogram<sup>126</sup>. Sometimes, alignment and reconstruction can be applied iteratively to improve the quality of the alignment. For example, using the simultaneous iterative reconstruction technique (SIRT) algorithm, it can re-project the reconstructed tomogram and compare with the original projections to calculate the misalignment of 2D image stack<sup>127</sup>.

### 3.3. Reconstruction

The mathematical formulation of tomographic reconstruction is based on the Radon Transform<sup>128</sup>. The Radon transform can transform the real space data in (x, y) coordinates system to its Radon space which is in (θ, t) coordinates system. From the Radon transform, a projection can be defined as a collection of several line integrals. These parameters are defined as a line:

$$x \cos(\theta) + y \sin(\theta) = t \quad (3.3.1)$$

The function  $R(\theta, t)$  is called the Radon transform of the function  $f(x, y)$ . It was first studied by Johann Radon in 1917. The formulation of Radon transform can be represented by transforming the function of  $f(x, y)$  through an

object to the function which has the parameters  $\theta$  (tilting angle) and  $t$  in Radon space.

$$R(\theta, t) = \int_{(\theta, t)} f(x, y) ds \quad (3.3.2)$$

The process of the Radon transform is illustrated in **Figure 14** in which a simple example of Radon transform of a 2D square is given. The four large values at the marked coordinates,  $(\theta_1, t_1)$ ,  $(\theta_1 + \pi/2, t_1)$ ,  $(\theta_1, t_2)$ ,  $(\theta_1 + \pi/2, t_1)$ , in Radon space (in **Figure 14d**) represent the four straight lines making up the sides of the square in real space. The marked points shown in Radon space give both the orientation of the lines and their distances to the center of the square. The four marked points have larger value because when the electrons passing through the straight lines in the square are strongly scattered.

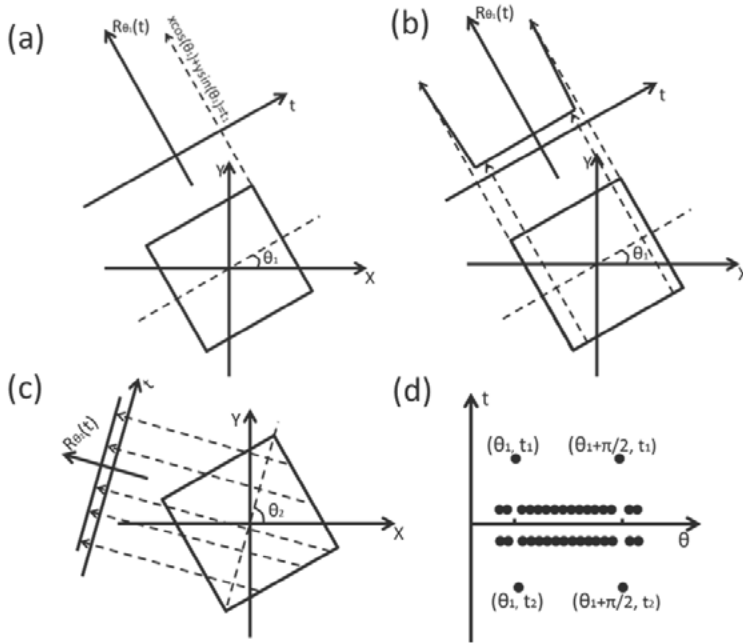


*Figure 14: Radon transformation of a 2D square in real space. (a) Line integral  $R_{\theta_1}(t)$  through an object  $f(x, y)$  which is presented by a square. (b) Parallel projection  $R_{\theta_1}(t)$  of an object  $f(x, y)$  consisted of a set of line integrals. (c) Parallel projection  $R_{\theta_2}(t)$  of an object  $f(x, y)$  at tilted angle,  $\theta_2$ . (d) the representation of a square in the Radon space.*

The type of projections is required to be parallel projections, other types of projections such as fan beam or cone beam projections are not considered in

electron tomography. Many imaging techniques in TEM provide such parallel projections, at least to a good approximation.

Now, the question is can we directly find the function  $f(x, y)$  by knowing the function of  $R(\theta, t)$ ? The answer is yes, the inverse Radon transform by assuming that the original image is made of straight lines can give back the function  $f(x, y)$ , but with low accuracy due to the complexity of the original image. Therefore, another method is introduced into the reconstruction procedure which is called Fourier slice theorem.

The central Fourier slice theorem describes the relationship between the Radon transform and the Fourier transform of a 3D object. It is the basis for all data acquisition and reconstruction procedures in electron tomography. In the central Fourier slice theorem, the 1D Fourier transform  $U(\theta_1, \omega)$  of a projection  $R_{\theta_1}(t)$  is equal to a central slice through the 2D Fourier transform  $F(u, v)$  of the original object  $f(x, y)$  at an tilting angle of  $\theta_1$ . Mathematically, it was written as:

$$F(u, v) = \iint_{-\infty}^{\infty} f(x, y) e^{-i2\pi(ux+vy)} dx dy \quad (3.3.3)$$

$F(u, v)$  is the 2D Fourier transform of an object  $f(x, y)$ . And the Fourier transform  $U(\theta, \omega)$  of a projection  $R(\theta, t)$  is:

$$U(\theta, \omega) = \int_{-\infty}^{\infty} R(\theta, t) e^{-i2\pi\omega t} dt \quad (3.3.4)$$

According to the central slice theorem<sup>129</sup>, the Fourier transform of a projection is equal to a central slice through the 2D Fourier transform of the object, so it can be written as:

$$U(\theta, \omega) = F(\omega \cos\theta, \omega \sin\theta) \quad (3.3.5)$$

The projections acquired at different tilt angles give information about the Fourier transform of the 3D object along central slices. If enough projections are acquired, the full information about the object can be recovered. In principle, the direct Fourier reconstruction methods can be done by an inverse Fourier transform in 2D<sup>130</sup>. However, it requires an interpolation of the discrete data in Fourier space when transforming these data from polar coordinates to Cartesian coordinates, which will bring errors. Therefore, it is preferred to reformulate the problem in a way which requires an interpolation in Radon space rather than in Fourier space.

Let us now look at the formula for the inverse Fourier transform in Cartesian coordinates system:

$$f(x, y) = \iint_{-\infty}^{\infty} F(u, v) e^{-i2\pi(ux+vy)} du dv \quad (3.3.6)$$

Substituting the Cartesian coordinates by polar coordinates system, it gives:

$$f(x, y) = \int_0^{2\pi} \int_{-\infty}^{\infty} U(\omega, \theta) |\omega| e^{-i2\pi\omega t} d\omega d\theta \quad (3.3.7)$$

Since the projections from  $0^\circ$  to  $180^\circ$  are equal to projections required from  $180^\circ$  to  $360^\circ$  and the central slice theorem can be expressed as:

$$f(x, y) = \int_0^\pi \int_{-\infty}^\infty U(\omega, \theta) |\omega| e^{-i2\pi\omega t} d\omega d\theta \quad (3.3.8)$$

This is the formula for the backprojection reconstruction, the whole backprojection process can be described by two parts. The double integral can be divided into two, one can be represented as the backprojection operation, which can be written as:

$$f(x, y) = \int_0^\pi Q(\theta, x\cos(\theta) + y\sin(\theta)) d\theta \quad (3.3.9)$$

Back projection is a process simply runs the projections back through the image and obtain the approximately original object. It is clear that the contributions from the low frequency signals are overestimated due to the over sampling close to the center of the Fourier space, weighting is necessary to equalize the impact of different frequency components. This is often called as weighted back projection or filtered back projection which was represented by the other integral in formula.

$$Q(\theta, t) = \int_{-\infty}^\infty U(\omega, \theta) |\omega| e^{-i2\pi\omega t} d\omega \quad (3.3.10)$$

This operation  $Q(\theta, t)$  is sometimes called filtered backprojection, or weighted backprojection by applying a filter  $|\omega|$  in Fourier space. The filtering is necessary because the data is always more densely sampled at the low frequencies, but loosely sampled at the high frequencies, and filtering or weighting can make data from both low and high frequency domain equally sampled.

The central slice theorem allows estimating the possible resolution in tomography and understanding artifacts, which appear in the reconstruction. The 3D resolution is different along different directions of space and depends on the original resolution of the imaging technique as well as on acquisition parameters of the projections. In this section, we will consider only the effect of acquisition parameters, such as the number of projections, on the resolution of the reconstruction.

Let us consider the resolution of the reconstructed tomograms, to simplify the case, we can assume that the resolution of the individual projections is limited only their pixel size. Projections with an image size  $W \times W$  and a number of pixels  $N \times N$  along 2D dimensions have therefore the 2D resolution of the individual projections is  $(W/N)^2$ . In the best case, the 3D reconstructed tomogram can then have the same resolution as the 2D projections along all three dimensions. However, in fact, the resolution in 3D dataset is generally anisotropic due to the imperfection of the reconstruction process.



We know that from the central slice theorem, each projection represents a central slice through the 3D Fourier transform of the object. To recover the 3D resolution of the reconstructed tomogram equal to the resolution of the 2D projections, it requires that the spacing between central slices is smaller than the voxel size of the 3D Fourier transform of the objects at least in the central sphere of the Fourier transform. To fulfill this, the number of projections  $n$  required to reconstruct a volume with a size of  $N \times N \times N$  when the projections have a size of  $N \times N$  can be expressed as:

$$n_{proj} = \frac{N \cdot \pi}{2} \quad (3.3.11)$$

This means that if the 2D projections are equally spaced over a range of  $180^\circ$  and have the same resolution between 2D projections and 3D tomogram, approximately, 1600 projections with a size of  $1024 \times 1024$  pixels are needed. It then needs the sample to be tilted with very small angular intervals which is difficult to be achieved in practice. In reality, the typical tilting intervals are one degree or few degrees, resulting in 180 projections or less depending on the capability of the tilting range. A resolution limit due to this effect was formulated (3.3.12) by the Crowther criterion<sup>131</sup>, and it gives the resolution of an object in the diameter of  $D$  in XY plane of which does not contain missing wedge.

$$d_x = \frac{D \cdot \pi}{n_{proj}} \quad (3.3.12)$$

Another limitation in the resolution of electron tomography is due to the missing wedge effect shown in **Figure 15**. Due to the geometric limitations of the sample or the sample holder, the full tilting range of  $180^\circ$  is often not able to achieve. This leads to the missing part which has a wedge-shaped part in the Fourier domain. The missing of the information leads to an elongation of reconstructed objects in the direction of the missing wedge.

The elongation factor is expressed as follows to quantify the elongation of a single point (point spread function) in the reconstruction along the z direction<sup>132</sup>.

$$e_{xz} = \sqrt{\frac{\alpha + \sin \alpha \cos \alpha}{\alpha - \sin \alpha \cos \alpha}} \quad (3.3.13)$$

$\alpha$  is the maximum tilting angle in radians. Depending on the maximum tilting angle, the degradation of the resolution in z direction can be expressed as a function of the resolution in x direction as

$$d_z = e_{xz} d_x \quad (3.3.14)$$

The elongation factors in single and double tilt was calculated from the above formula and compared by Mastronarde and coworkers<sup>118</sup>. For exam-

ple, if the sample was tilted from  $\pm 60^\circ$  and then projections were collected from a single tilt series, then the elongation factor is about 2.5 which indicates that in the direction of the missing wedge resolution is 2.5 times worse than outside of the missing wedge. However, if the tilt series is acquired by double tilt series, then the elongation factor is about 1.8 which is better than the single tilt series.

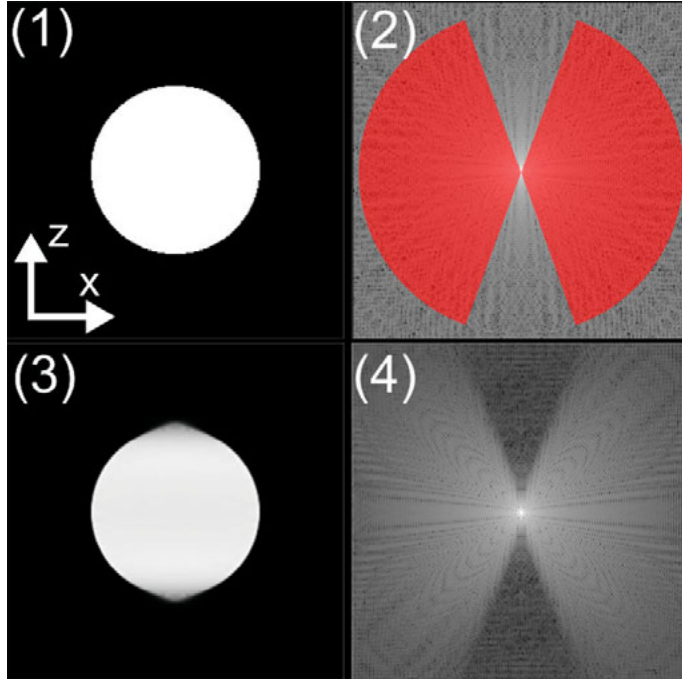


*Figure 15: The elongation effect due to the missing wedge artefact. (1) the original image, (2) FFT of the original image, (3) the reconstructed sphere, (4) FFT of the reconstructed sphere.*

### 3.4. Segmentation and post processing

The most commonly used post processing algorithms in electron tomography are iterative algebraic methods, most frequently the simultaneous iterative reconstruction technique (SIRT) <sup>133</sup> as well as other variants of similar techniques such as the simultaneous algebraic reconstruction technique (SART) <sup>134</sup>. These post processing techniques can generally reduce the impact of artifacts coming from the limited number of projections and the missing wedge.

It is also considered as an advantage to use a filter before segmentation to reduce noise. A large number of filters known in image processing can be applied for this task. Filters, such as anisotropic diffusion filters <sup>135,136</sup>, are

frequently used in electron tomography. These filters are iterative filters, based on gradient measures and on conduction coefficients calculated from these gradient measures, which weight how strong each neighboring value changes a specific value in each iteration.

A large number of possibilities exist for segmentation. Segmentation can be done manually, semi-automated or fully automated. A problem with manual methods is their subjectivity, which can make results dependent on the person performing the segmentation. However, they are still frequently employed as human experience can often identify sample features better than computer vision.

The simplest method for segmentation is to do the segmentation based on absolute threshold values. The simple threshold method is based on the assumption that all the voxels that below a certain threshold value are attributed to one phase, while all voxels above the threshold are attributed to another phase. The chosen threshold value can be based on the grey values of the region which is detected as edge of the object of interest. Apart from such global thresholding methods there exist also methods using local thresholds, which are useful, if the image intensity varies between different regions.

In this chapter, the principles and relevant techniques for electron tomography are discussed. The main goal of the tomographic reconstruction is to produce best reconstruction from available data. Meanwhile, the methods to overcome or compensate the practical limits are discussed, such as missing wedge artifact. Two approaches are suggested: dual- or multiple-axis tomography and the development of post processing algorithms.

### 3.5. Conclusion

Two major questions should be taken into consideration when choosing a signal to develop the electron tomography: (i) whether the chosen contrast mechanism fulfils the projection requirement; (ii) whether the chosen contrasts can provide good understanding to the materials related questions. After these two considerations, other important questions, for example, the total acquisition time, electron dose, sample stability, alignment of the image stack, reconstruction, segmentation and post-processing, should be concerned as well. For the high temperature annealed SRSC sample, EFTEM imaging using the plasmon signals generally fulfils the projection requirement and can provide the desired information that is closely related to the growth mechanism of nanostructures. The detailed discussion on the correlation between the 3D analysis of Si NPs and growth mechanism is given in **Chapter 4**. For the life science sample, the BFTEM signal meets the projection requirement, but the electron dose and sample stability were concerned

when taking the tilt series. The detailed electron tomography analysis on hIAPP protein aggregates is discussed in **Chapter 5**.

## 4. Electron tomography analysis on the absorber layer of all-Si tandem solar cells

The size of NPs and the spacing between the adjacent NPs in three dimensions has been considered as an important parameter which can influence the transport properties of the excited carriers<sup>14</sup>. In last 10 years, electron tomography technique with nanometer resolution was applied to precisely determine the 3D morphology of nanostructures (**Table 1**). The analysis on the morphology and the spacing between the synthesized Si NPs has become an appealing research topic in the field of the Si NPs based absorber layer.

The samples investigated by electron tomography were synthesized by wet process, CVD deposition and high temperature annealing process (listed in **Table 3**). The analysis goals of applying electron tomography on these samples are: (i) to measure the 3D density of Si NPs synthesized by wet process and CVD deposition using the BFTEM imaging based electron tomography; (ii) to characterize the precipitated nanostructures in the annealed SRSC film using the EFTEM SI imaging based electron tomography.

### 4.1. Bright field tomography

To understand the 3D distribution of Si NPs deposited by CVD process, electron tomography was applied. The Si NPs growth was performed by thermal decomposition of silane ( $\text{SiH}_4$ ) in hydrogen environment at 700 °C for 20 seconds under a total gas pressure of  $2.7 \times 10^3$  Pa in LPCVD chamber. During the 20s annealing at 700 °C, the Si NPs were formed on a 10 nm thick amorphous SRSC film which was previously deposited by PECVD method. From the SAD pattern (**Paper IV**), the formation of discrete spots like pattern instead of continuous ring like pattern indicates the crystallinity of Si NPs is rather low. In HRTEM images, only one Si NPs shows clear lattice fringes in every ten imaged NPs. Thus, the mass-thickness contrast of Si NPs dominates in the BFTEM imaging so that it is applicable for the development of electron tomography. The size distribution of Si NPs (measured from the isolated ones in 2D BFTEM image) is about  $4.8 \pm 0.7$  nm in diameter which can be approximated as a Gaussian distribution. Those Si NPs seem to be interconnected were neglected when measuring the size of the Si NPs. To overcome this overlapping effect in 2D images, Electron tomography using the BFTEM images was applied to analyze the size and distribution of Si NPs deposited by CVD method.

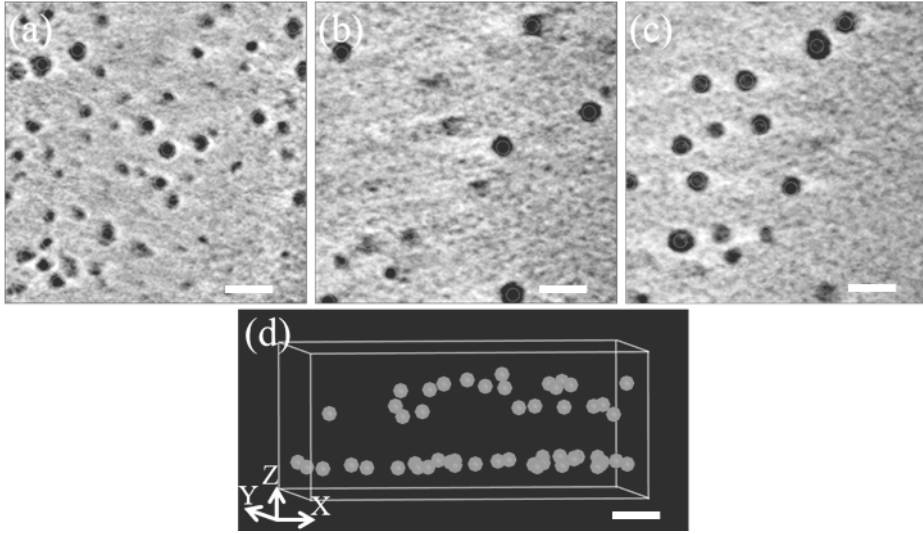


*Figure 16: Electron tomography analysis on the CVD deposited Si NPs. (a)-(c) three slices extracted from the reconstructed tomogram in an order of bottom, middle and top. (d) 3D view of the distribution of Si NPs, the green markers are placed onto the center of mass of the Si NPs observed from the reconstructed tomogram. The scale bars are 10 nm.*

In **Figure 16**, the electron tomography analysis shows a 3D distribution of NPs. The tilt series was acquired in the BFTEM imaging condition from the  $60^\circ$  to  $-60^\circ$  with  $2^\circ$  as increment. The tilt series was aligned and reconstructed from a single tile series using the IMOD software package<sup>118,137,138</sup>. In the three slices (**Figure 16(a)-(c)**) extracted from the reconstructed tomogram, the crystalline Si NPs appear as dark dots like contrasts with various sizes. The size of the Si NPs was determined by measuring the diameter of 41 selected Si NPs appeared in the extracted slices. The measured size distribution from the 3D data is shown in **Figure 17**, which is equal to  $4.0 \pm 1.5$  nm, instead of having a symmetric distribution, the measured size distribution shows a clear broadened shoulder above the average size of NPs. This is similar to the reported asymmetric size distribution due to the ripening effect of NPs<sup>28</sup>.

In fact, neither of the top nor bottom slice shows a uniform size distribution of NPs which indicates a 3D ripening process occurred during the 20s annealing. More interestingly, the Si NPs are sitting on the top layer seem to have a larger average size than the ones are located at the bottom layer that is near to the amorphous Si rich SiC film. The Si NPs were deposited denser at the bottom layer than the top layer as shown in **Figure 16(d)**.

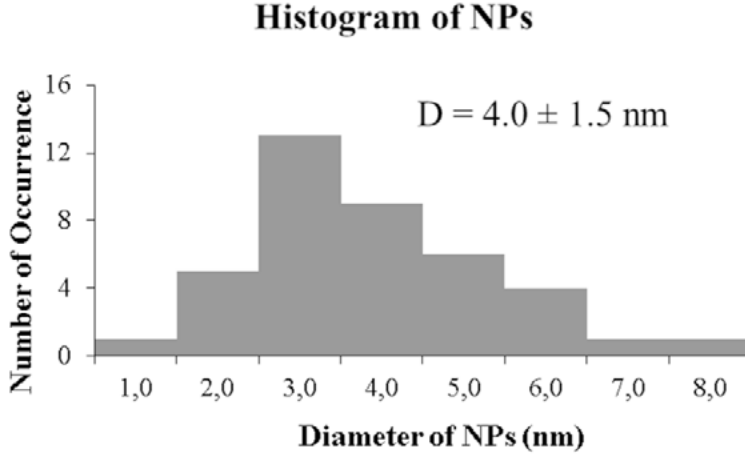


*Figure 17: The size distribution of Si NPs synthesized by CVD process measured from the extracted slices in Figure 17.*

The Si NPs synthesized by wet process were also analyzed by electron tomography technique using BFTEM images. The detailed description of the Si NPs synthesis, the deposition of the absorber layer and a series of annealing processes in different environment was described in **Paper I**. In this absorber layer, the Si NPs were embedded in the ITO matrix. The conventional 2D TEM characterization techniques, such as BFTEM imaging, HRTEM imaging and SAD patterns, were applied to measure the size distribution and crystalline phase of Si NPs in **Paper I**. In the SAD pattern, the reflection signals generated from the crystalline Si is relatively low and form discrete spots instead of continuous rings. Thus, in wet chemical process, the mass-thickness contrast of Si NPs dominates in the BFTEM imaging and electron tomography was developed based on BFTEM images to study the distribution of Si NPs (**Paper I**). The size distribution of the isolated Si NPs measured from the BFTEM is  $3.1 \pm 0.8$  nm.

Using electron tomography, the 3D distribution of Si NPs was studied. A single tilt series was acquired in BFTEM imaging mode from the  $60^\circ$  to  $-60^\circ$  with  $1^\circ$  as increment. The Si NPs were shown as dark dots like contrasts in **Figure 18(a)-(c)**. The size distribution NPs were measured from 65 NPs shown in the **Figure 18(a)** and the size distribution is  $3.4 \pm 0.9$  nm, which is the same to the value measured from the BFTEM. However, from the BFTEM images, the center to center spacing of Si NPs can not be precisely determined due to the overlap and projection effects. The distance can be measured from the tomographic data in **Figure 18(b) and (c)**. In (b) and (c), the distribution of NPs along the Z direction can be visualized and the center to center distance can be easily measured. As discussed in **Chapter 1.3**, the

spacing between NPs is an important parameter to understand the carriers transport between the nearest NPs. By analyzing the reconstructed tomogram, the averaged spacing between the nearest NPs is about 8.3 nm and the 3D density of NPs is  $1.6 \times 10^{18} \text{ cm}^{-3}$ .

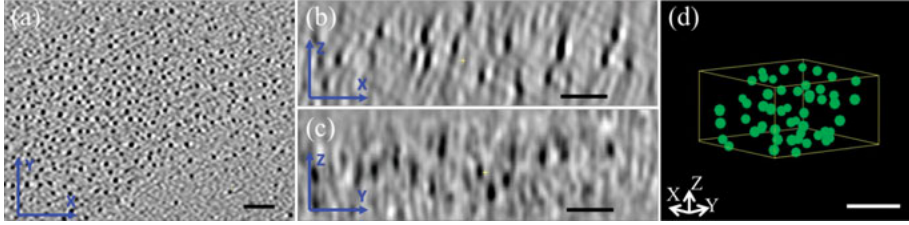


*Figure 18: Electron tomography analysis of Si NPs synthesized by wet process. (a)-(c) are the XY, XZ and YZ slices of the reconstructed tomogram, respectively. (d) 3D view of the distribution of Si NPs, the green markers are placed onto the center of mass of the Si NPs observed from the reconstructed tomogram. The scale bars are 20 nm.*

## 4.2. EFTEM SI tomography

The growth of Si NPs synthesized by high temperature annealing process follows a different formation mechanism from the wet process and CVD method. In the wet process, the Si NPs and ITO matrix were firstly prepared separately, and then mixed up to deposit a nanocomposite used for the absorber layer by AACVD technique. The high temperature annealing treatment (in the forming gas environment at 300 °C) in wet process is routinely used to decrease the resistivity of ITO by reducing the density of defects at grain boundaries<sup>90</sup>. In the CVD method, the growth of Si NPs was governed by the thermal decomposition of  $\text{SiH}_4$  precursor in hydrogen at 700 °C, the nucleation of Si NPs was strongly related to the surface chemistry of the amorphous SiC surface. Both of these processes do not involve in the precipitation process of NPs from the parental matrix. In the high temperature annealing process, Si NPs are formed from the SRSC films during the annealing. As discussed in **Chapter 1.3**, depending on the content of excess Si, either nucleation and growth or spinodal decomposition processes governs the formation mechanism of Si NPs from the SRSC films. From the ERDA analysis, the composition of the targeted SRSC film is  $\text{Si}_{0.67 \pm 0.02} \text{C}_{0.33 \pm 0.02}$ . The excess Si is about 34 at. %, thereby a spinodal decomposed Si network structure would be expected after the annealing process. From the 2D EFTEM images, Si appears as interconnected structures and a-SiC seems to distribute as an interface between Si network structure and 3C-SiC NPs.



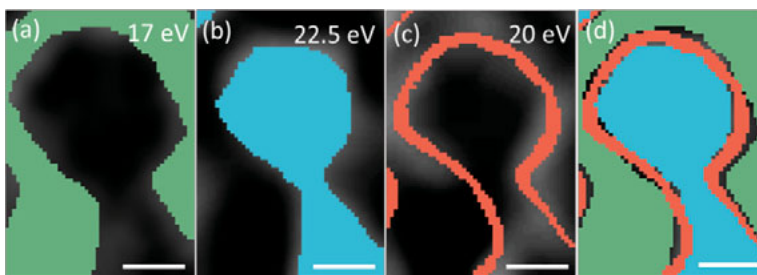


*Figure 19: Segmentations performed on the reconstructed tomograms. The segmentations were applied on the reconstructed tomograms using: (a) Si plasmon signal (in green color), (b) 3C-SiC plasmon signal (in blue color), (c) a-SiC plasmon signal (in red color). A combined segmentation is shown in (d). The scale bars are 5 nm.*

The acquisition and formation of 2D EFTEM images were discussed in **Chapter 2.2.2**. The image stack was generated by tilting the sample from the  $60^\circ$  to  $-60^\circ$  with  $3^\circ$  as increment. A double tilt series was acquired for the purpose of reducing the elongation effect. Since the contrasts presented in the 2D plasmon images are sufficient for the image stack alignment and tomographic reconstruction, no filtering was applied on the raw 2D images before the alignment and reconstruction. The alignment of the plasmon image stacks was carried out using the markerless alignment method with an error residue of 2 pixels. The segmentation was performed by choosing a threshold intensity at which the contours were represented in colors (see **Figure 19**). In the reconstructed tomograms, the signals themselves have soft outlines, as expected from the delocalization of plasmon scattering. Therefore, we set up a threshold value to avoid choosing the diffused signal ( $\sim 1$  nm) and the similar segmentation method was also applied on rendering the tomographic data reconstructed by using the plasmon signal<sup>13</sup>.

From the segmented sub-volumes, the 3D distribution of Si, a-SiC and 3C-SiC were presented in **Figure 20**. The detailed discussion on each sub-volume can be found in **Paper VII**. Briefly, Si has a morphology of interconnected columnar like structure, thereby it looks like a network structure from the 2D projection. The columnar regions that are surrounded by several 3C-SiC NPs take larger fraction than the connecting regions which are located at the grain boundaries between two 3C-SiC NPs. The 3D computational simulation on the spinodal decomposition process of a binary system has shown the similar interconnecting columnar structure as in the later stage of the spinodal decomposition process<sup>32</sup>.

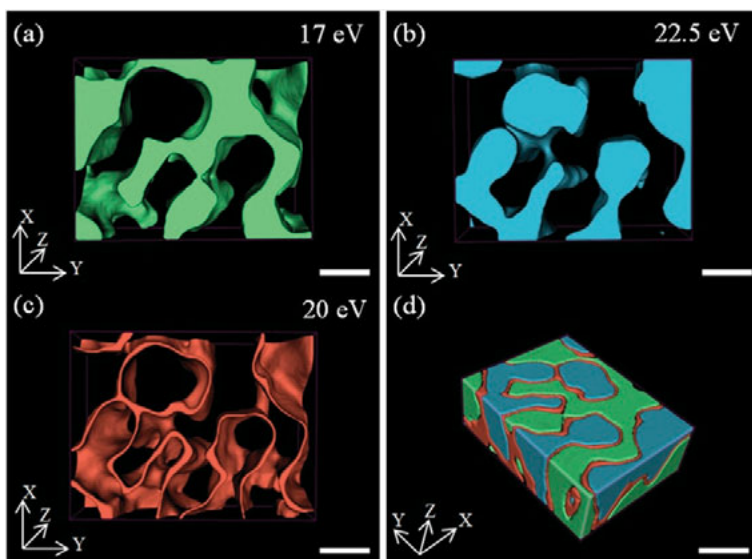


Figure 20: Electron tomography analysis of 1 hour annealed SRSC film. (a)-(c) are the sub-volumes of Si network structure, 3C-SiC NPs and a-SiC interface, respectively. (d) the combined sub-volumes of (a), (b) and (c). The scale bars are 10 nm.

The formation of the a-SiC interface can also be explained as a result of the spinodal decomposition process. In the studied SRSC film, the excess of Si is about 34 at. %, thereby a spinodal decomposed Si-SiC nanocomposite would be expected. In the region SiC phase which has a stoichiometric composition, cubic 3C-SiC crystalline phase can be precipitated according to the phase diagram of Si-C<sup>139</sup>. Among the polytypes of the crystalline SiC phases, the 3C-SiC phase is thermodynamically more stable than the hexagonal form of SiC at any temperature below the peritectic point ( $2545 \pm 40$  °C)<sup>139</sup>. The observation of only 3C-SiC crystalline phase formed in annealed SRSC has a good agreement with previous studies in which only 3C-SiC NPs has been reported<sup>38,39</sup>. Since the precipitation of the NPs needs to grab atoms diffused from the surrounding matrix, this leads to the formation of a metastable diffusion layer structure near to surface of the precipitated NPs<sup>29</sup>. In the studied case, the precipitation of 3C-SiC NPs leads to the formation of the metastable a-SiC phase at the interfacial region. In the Si-C phase diagram, such a metastable a-SiC phase can be predicted when the composition of C is in a range of 39 at. % ~ 61 at. %<sup>139</sup>. The STEM-EELS SI using the core-loss signals of Si-L edge and C-k edge also indicates that the relative atomic composition of Si to C at the interface is 50 at. %  $\pm$  10 at. % (**Chapter 4.3**).

### 4.3.4D electron tomography

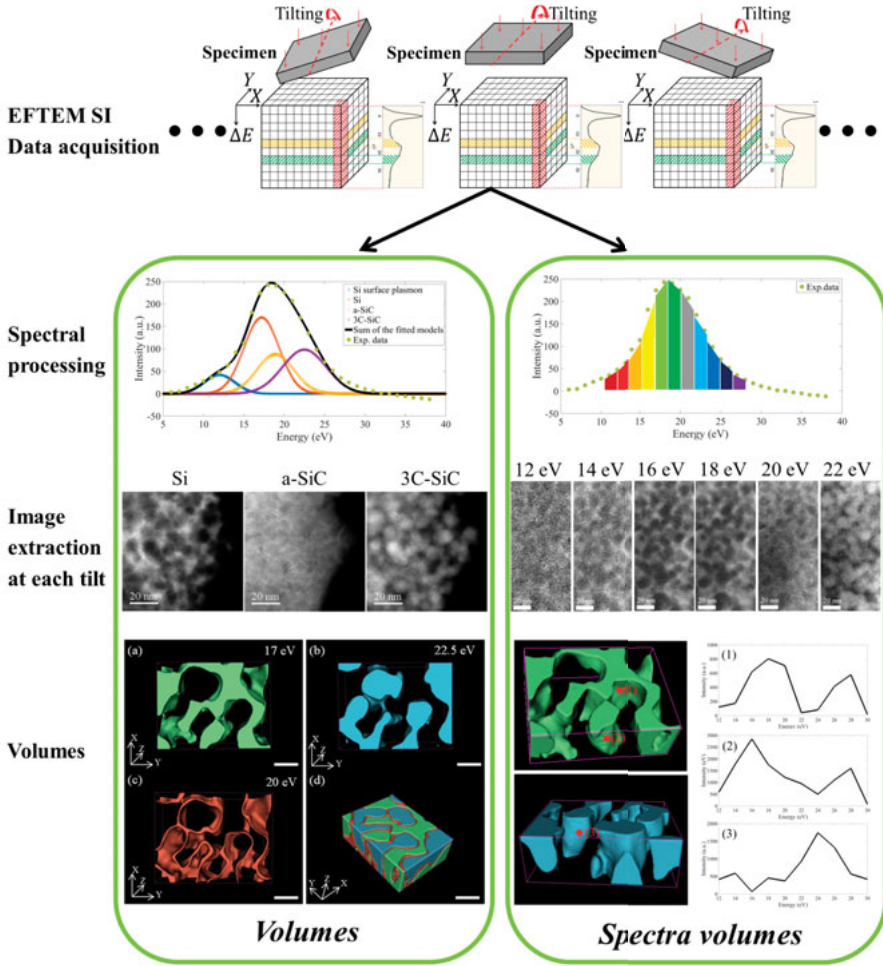


Figure 21: The sketch shows two methodologies to develop the analytical electron tomography in this thesis.

In the last chapter, the 3D elemental characterization by using the bulk plasmon signals of Si, a-SiC and 3C-SiC has been demonstrated. First, the reference plasmon spectra of Si, a-SiC and 3C-SiC were proposed; secondly, the corresponding plasmon images were extracted by fitting the reference plasmon spectra. We then obtain three different tilt series, one for each plasmon image. Finally, the whole volume of the annealed SRSC film was reconstructed separately for the three different tilt series: Si, a-SiC and 3C-SiC. In the reconstructed sub-volumes, the 3D distribution of Si, a-SiC and 3C-SiC are clearly shown, though in this case, no low-loss spectrum can be extracted from the individual voxels. There are noticeable fitting residues at around 28 eV (shown in **Figure 8**) which was neglected during the fitting procedures

and this could be the volume plasmon energy of graphitic carbon<sup>93</sup>. The distribution of the graphitic carbon remains unclear in the reconstructed sub-volumes.

Since the signal to noise ratio in our original low loss Sis is rather high, we propose another method to treat the EFTEM SI dataset as described in the right green frame in **Figure 21**. In this method, instead of using reference plasmon models, we carried out the tomographic reconstruction for all the 10 images in the series of EFTEM images ranging from 12eV to 30eV acquired with a 2 eV energy slit. Then, a tomogram can be reconstructed by collecting EFTEM images at the same energy loss through a tilt series. By reading the intensity values at the same voxel from 10 tomograms, a low-loss spectrum (in the range of 12 eV to 30 eV) can be reconstructed at each voxel. This means, that similar to the spectrum-imaging technique, one can extract now a spectrum at each pixel, in this case, each voxel in the volume contains a spectrum that can be reconstructed from the tomograms (illustrated in **Figure 21**).

This method was called as “spectra-volumes” imaging technique or four dimensional (4D) electron tomography technique<sup>70,79–82</sup>. Gass and coworkers have applied 4D electron tomography technique to study the interfacial structural and chemical composition of the multi-walled carbon nanotubes and nylon composite<sup>82</sup>. Haberer and coworkers extended the capabilities of conventional electron tomography to 3D localized elemental analysis by extracting the signals from the energy-dispersive X-ray (EDX) spectroscopy, low-loss and core-loss EELS at each voxel in 3D<sup>70</sup>. Goris and coworkers have performed the reconstruction on the raw EELS data and the reconstructed spectra can spatially resolve the valence states of Cerium ions in its oxide compound<sup>79</sup>. In general, 4D electron tomography allows reconstructing local chemical information (EDX or EELS spectra). Some of these reported methods use actually prior data treatment of the acquired spectrum image data cubes in the tilt series, in most cases statistical methods such as principal component analysis. Though this might be reasonable in order to reduce noise in the data at an early stage of the process, in turn this means that prior choices were made that can make it difficult to follow a real spectroscopic signal through all data treatments needed in the process of tomography. We proposed and apply here are 4D tomograms based on raw data and whose only artifact comes from the artifacts in the tomographic reconstruction process.

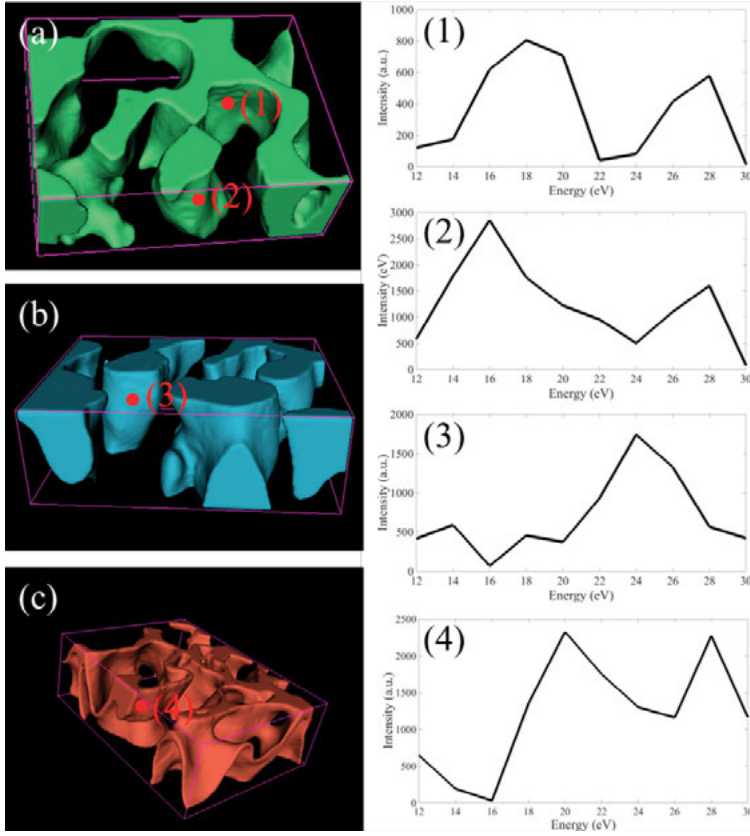


Figure 22: The reconstructed single voxel spectra (voxel size:  $1 \text{ nm}^3$ ). (a) Si network structure; (b) 3C-SiC NPs; (c) a-SiC interface. (1)-(4) are the reconstructed low-loss spectra extracted from the voxels indicated red spots in (a)-(c). The volume size in (a)-(c) is  $X (60 \text{ nm}) \times Y (45 \text{ nm}) \times Z (20 \text{ nm})$ .

**Figure 22** shows spectra extracted from the sub-volumes, the spectra were locally extracted from one voxel marked by the red dot in **Figure 22(a)-(c)**. One apparent benefit of the reconstructed spectra compared to the reference spectra is that the reconstructed spectra can avoid superposition effects during the acquisition of the 2D spectra so only the contributions from the localized voxel were extracted in the reconstructed spectra. The reconstructed spectra (1) and (2) were extracted from the Si network region shown in **Figure 22(a)**, one significant feature that the reference spectrum of Si does not carry is the additional plasmon peak at 28 eV which corresponds to the graphitic carbon<sup>93</sup>. Another interesting observation is that the Si plasmon peak shifts from 18 eV to 16 eV by comparing the reconstructed spectra (1) and (2).

The plasmon peak shift from 16 eV to 18 eV can be explained by the formation a-Si and c-Si NPs. When analyzing the Si precipitates embedded in the Si network structure using the EFTEM imaging technique, it is difficult to distinguish a-Si (at 16.4 eV<sup>93</sup>) and c-Si (at 16.7 eV<sup>93</sup>) phases because the plasmon peak of these two phases are too close to be separated<sup>12,16,18</sup>. Note that the reconstructed low-loss EELS spectra have only an energy resolution of 2 eV which corresponds to the energy slit used for the acquisition of the EFTEM SI dataset. The shift of the plasmon peak shown in (1) and (2) is 2 eV (from 18 eV to 16 eV) and the plasmon energy of 18 eV at point (1) may indicate the presence of the c-Si. Due to the quantum confinement effect, the plasmon energy of small c-Si NPs can shift to higher energies, for example, 3.5 nm c-Si NP has a plasmon energy of 17.5 eV<sup>109</sup>. Thus, at the point (1), there is maybe a 2 nm c-Si NP which has a plasmon energy of 18 eV. At the point (2), the plasmon energy of 16 eV corresponds to a-Si NP. The reconstructed low-loss spectra (from 12 eV to 30 eV) at the Si network region reveal the existence of C and could help identify the a-Si and c-Si NPs having a difference in plasmon energies larger than 2 eV.

At the points (3) and (4), the reconstructed spectra were extracted at 3C-SiC and a-SiC regions. The plasmon peak seen from the point (3) was generated from the 3C-SiC NP at about 24 eV. At the point (4), two plasmon peaks at 20 eV and 28 eV were observed which indicate the presence of a-SiC and graphitic C. This is also expected, because the metastable phase of a-SiC can be formed when the atomic concentration of C ranges from 39 at. % to 61 at. %<sup>139</sup>. Therefore, when the concentration of C in Si is over 50%, then both a-SiC and C can be coexisted.

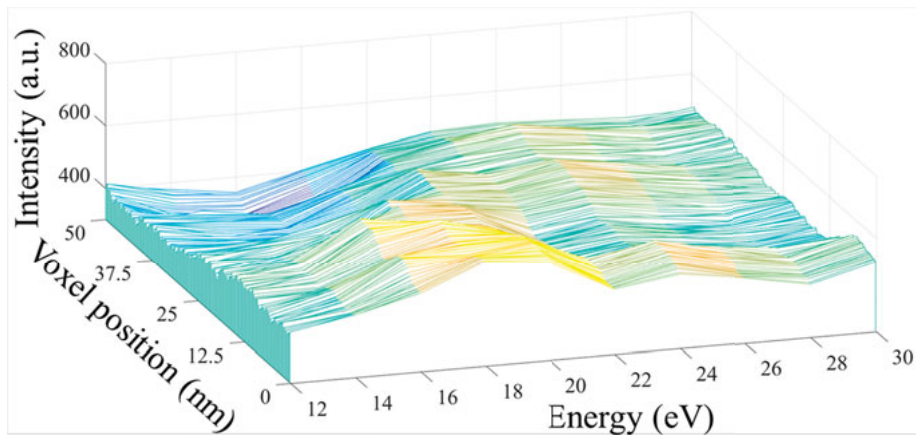
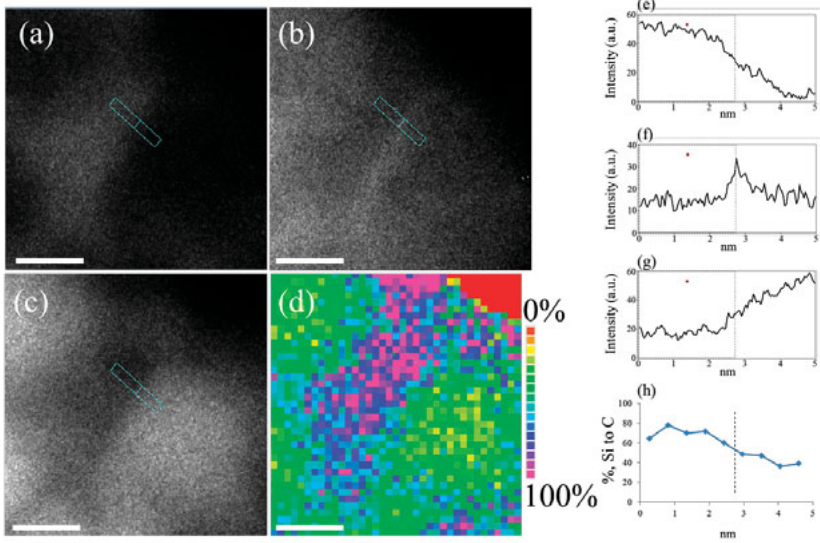


Figure 23: The reconstructed single voxel spectra across a line containing both Si, a-SiC and 3C-SiC nanostructures (voxel size: 0.25 nm × 0.25 nm × 0.25 nm in XYZ).



In principle, in a volume of  $54000 \text{ nm}^3$  (in **Figure 22**) with voxel size of  $0.25 \text{ nm} \times 0.25 \text{ nm} \times 0.25 \text{ nm}$  in X,Y and Z respectively, more than three millions of spectra can be extracted from each voxel. Now, the statistical analysis on these millions of spectra is still under processing and evaluation. In **Figure 23**, 200 spectra were presented voxel by voxel across the regions of Si network to 3C-SiC NPs and the shift of the plasmon peak from 16 eV to 18 eV, 20 eV and 24 eV are clearly observable.



*Figure 24: The compositional fluctuation of Si respected to C at the regions of the Si network like structure, a-SiC and 3C-SiC NPs. The plasmon images of Si, a-SiC and 3C-SiC shown in (a), (b) and (c) were acquired from the same area as in (d). The STEM-EELS core-loss mapping in (d) was acquired using the Si-L edge and C-k edge signals to show the relative compositional fluctuation of Si to C. The pixel size of the STEM-EELS mapping is  $0.5 \text{ nm} \times 0.5 \text{ nm}$ . The scale bars are 5 nm. The intensity profiles and compositional profile were extracted from the regions of interest (ROIs) marked by the rectangular areas in (a)-(d). The dash dark lines in (e)-(h) indicate the position of the a-SiC interface.*

In fact, the existence of C in the Si network structure was also verified by the 2D STEM-EELS SI mapping using the Si-L edge and C-K edge core loss signals (**Figure 24**). The plasmon images (**Figure 24(a-c)**) and STEM-EELS mapping (**Figure 24(d)**) were acquired from a region on which has a thickness about 8 nm, thereby the overlapping effect of the Si and SiC phases in those images can be assumed to be minimum due to the columnar like morphologies of Si, a-SiC and 3C-SiC seen from the **Figure 20**. The ROIs were chosen where the a-SiC is clearly distributed as the interface between the Si and 3C-SiC NPs in 2D plasmon images (**Figure 24(a-c)**). The max-

imum of the intensity profile extracted from the a-SiC plasmon signal was marked by the dark dashed line (**Figure 24(f)**). At the same position in the Si and 3C-SiC plasmon images, the dark dashed line was located at the approximate FWHMs of the intensity profiles extracted from Si and 3C-SiC plasmon signals in **Figure 24(e) and (g)** and at the boundaries of the bright contrasts in Si and 3C-SiC plasmon images **Figure 24(a) and (c)**. This indicates the distribution of the a-SiC as an interface between the Si and 3C-SiC at the ROIs. By combining the plasmon images of a-SiC (**Figure 24(b)**), STEM-EELS mapping (**Figure 24(d)**) and the relative compositional profile (**Figure 24(h)**), we can see that the thin a-SiC interface was located at the region where the relative Si to C composition is near to the stoichiometric SiC (50 at. %  $\pm$  10 at. %). This is in a good agreement with the phase diagram of Si-C, the metastable phase of a-SiC can be formed when the atomic concentration of C ranges from 39 at. % to 61 at. %<sup>139</sup>. By combining the plasmon images of Si (**Figure 24(a)**), STEM-EELS mapping (**Figure 24(d)**) and the relative compositional profile (**Figure 24(h)**), we can see the relative Si to C composition at some pixels is not reaching 100 at. %, which indicates the existence of C in the Si network structure.

#### 4.4. Conclusion

The 3D analysis can always provide important information that 2D images do not contain. For example, in our analyzed cases, the 3D density the spacing of small Si NPs can only be obtained for the electron tomography technique. By analyzing the 3D data, the overlapping and projection effects can be very well excluded resulting in a more precise measurement on the size of Si NPs. By adding one more dimension onto the 3D data, such as EELS spectral information, EFTEM SI shows the capability of analyzing the interfacial nanostructures formed in the high temperature annealed SRSC film (**Paper VII**). The observation of the interfacial nanostructures and the formation mechanisms is correlated in terms of thermodynamic concepts. The observation of the metastable a-SiC interface indicates the nucleation and growth of the 3C-SiC NPs does not reach the equilibrium condition after 1 hour annealing at 1100 °C. The 4D electron tomography analysis seems to provide more interesting information than conventional volume reconstruction, the feasibility of reconstructing spectra voxel by voxel has been demonstrated. The full interpretation of the reconstructed spectra is not being obvious and more advanced statistical analysis is needed to treat the reconstructed spectra. At least, it is clear enough to draw a conclusion that C was diffused into Si network region and such an invasion can influence the crystallization process of Si during the annealing. To our knowledge, there is no other experiments could provide such a highly spatially resolved 3D volume from which the chemical information can be obtained voxel by voxel.



## 5. Electron tomography analysis on the hIAPP protein aggregates

Electron tomography has been applied predominately in life science during last three decades. In 1968, DeRosier and Klug has formulated the general principles of reconstructing a bacteriophage tail in the helical symmetry from a series of 2D images<sup>60</sup>. In the same year, Hart produced a “polytropic montage” to study unstained biological material at high resolution<sup>59</sup>. In 1976, Hoppe and coworkers published a 3D visualization of a negatively stained macromolecular assembly using the tomographic reconstruction method<sup>140</sup>. The recent development and application of electron tomography in life science was summarized in the review articles<sup>64,141</sup>.

A number of diseases is believed to be associated with the aggregation of amyloid peptides (**Table 2**). The aggregated amyloid peptides appears as long fibrous structure *in vivo*<sup>142</sup>. During the last decade, TEM has been applied as a main instrument to resolve the detailed structural information on amyloid or amyloid like fibrils taken from human tissue samples<sup>47</sup>. The protein precursors of amyloid or amyloid like fibrils that may vary in size in their primary and secondary structures, TEM is an appropriate method to analyze them. The analysis on the *Drosophila melanogaster* genome has revealed that 77 % of human disease related to genes have a homologue in *Drosophila melanogaster*<sup>53</sup>. Thus, the *Drosophila melanogaster* has been used as a model to study the neurodegenerative diseases, for example, Alzheimer’s disease<sup>49,50</sup> and Huntington’s disease<sup>51</sup>. A ten or twenty years aggregation process of amyloid peptides that leads to the various diseases in human body can be greatly shortened in *Drosophila melanogaster* model due to the short lifespan (2 weeks to one month)<sup>143</sup>. Therefore, using the comparable short-lived model allows fast data acquisition *in vivo* in an effective and economic manner. The electron tomography technique on TEM enables a detailed 3D analysis on a subcellular level<sup>56,57</sup>, in this thesis, for the first time, the electron tomography technique was applied to study the 3D distribution of the hIAPP aggregates formed in the fat body cells in the *Drosophila melanogaster*.

### 5.1. 3D crystalline structural analysis

The detailed sample preparation can be found in **Paper VI**. In the case of developing the electron tomography experiment on the biological samples, one has to think about the radiation damage at first. Norlin and coworker have used 300 kV TEM (Tecnai F30) to image the similar amyloid peptides

with an electron dose approximately of  $2400 \text{ e nm}^{-2}$ <sup>144</sup>. In this work, the similar electron dose was applied to irradiate the sample for about half an hour before the image acquisition and during the tilt series acquisition the electron dose was lower to  $\sim 1500 \text{ e nm}^{-2}$ . A double tilt series was developed in order to reduce the elongation effect. The tilt series was acquired from  $\pm 60^\circ$  with  $2^\circ$  increments. We did not observe beam damages such as shrinkage, distortion or broken parts on the sample during the acquisition. During the data acquisition, the defocus was controlled in a range of  $800 \text{ nm} \pm 20 \text{ nm}$ . The images obtained under this defocusing condition generate adequate phase contrast for the subsequent alignment and reconstruction. Also, the first zero of the contrast transfer function under this defocusing condition gives a spatial resolution of  $1.3 \text{ nm}$  in the XY plane and is sufficient to resolve the 3D structural information above  $3 \text{ nm}$ .

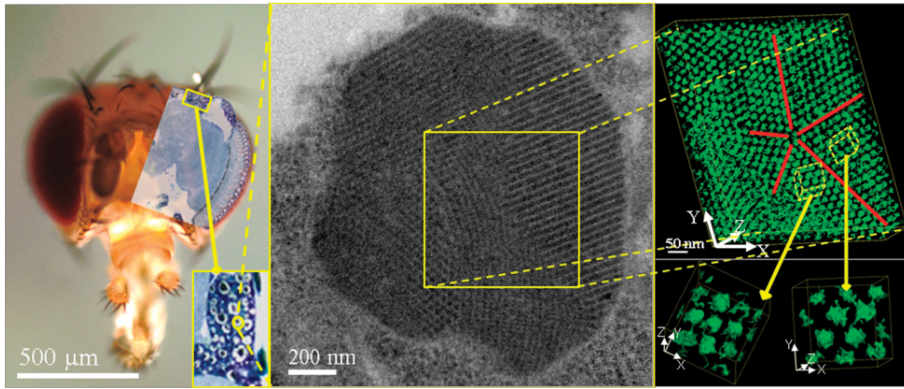


*Figure 25: (Left) Optical microscope images of a fly head, the inset image shown on the right bottom corner indicates the position of the fat body tissue in the fly head. The yellow solid circle indicates the position where the hIAPP aggregates may form. (Middle) TEM image of one hIAPP aggregate, (Right) 3D view of the hIAPP aggregation showing the crystalline structures constructed by the hIAPP protein granules and a 5-fold twinned structure was also observed.*

Combined with the optical microscopy and TEM images, the relationships between the function of the fat body tissue in fly brain and the 3D analysis on the hIAPP aggregate can be correlated as illustrated in **Figure 25**. The fat body tissue is unique to insects, and it is well known that this tissue can store large amounts of proteins that are used as nutrition during the developing stages when no feeding occurs<sup>145,146,147</sup>. It is difficult to judge if the hIAPP aggregate shown in the 2D TEM image has a tubular structure or a spherical structure. Only from our electron tomography analysis, it can be determined, that the hIAPP granules in our study have a close to spherical shape morphology.

Electron tomography analysis revealed that the aggregates were made up of granular subunits with a diameter of 20 nm aligned into a highly ordered structure in all three dimensions. The 3D lattice of hIAPP protein granules in the precipitates is constructed by two crystalline unit cells, the body centered tetragonal (BCT) in some parts of the aggregate and a triclinic unit cell in other parts. A 5-fold twinned structure was observed that is constructed by cyclic twinning of BCT and triclinic unit cells. The detailed discussions on the crystalline structure and 5-fold twinned structure formed in the hIAPP aggregate can be found in **Paper VI**. As far as we know, it is the first time to apply the electron tomography to analyze such a non-tubular amyloid like structure (or was also called as non-amyloid like structure <sup>148</sup>). Also, it is the first time to report the existing of 5-fold twinned structure in biology, however, the 5-fold symmetry was already reported in life science on the tricorn protease by using the electron tomography technique <sup>149</sup>.

## 5.2. Single particle analysis of hIAPP protein granules

The electron tomography technique is a 3D imaging technique where the data are obtained by tilting the specimen and collecting the 2D projections of the specimen. The conflict between the radiation damage and number of the tilts is known as a major limitation in biological 3D imaging using electron tomography technique. Single particle analysis was first developed to overcome this limitation by analyzing many 2D TEM images of the same biological object in random orientations <sup>150–153</sup>. Single particle analysis contains a group of computerized image processing techniques used to pick up the targeted particles from the 2D TEM images, then aligning the images and finally classifying the selected particles <sup>154</sup>, such analysis can be done on both negatively stained <sup>151</sup> and cryo-TEM samples <sup>155</sup>. Using the single particle analysis combined with further imaging processing and interpretation <sup>156</sup>, near atomic resolution 3D structural determination can be obtained from 2D cryo-TEM images on the macromolecular assemblies <sup>153</sup>.

In our case, the hIAPP aggregates are negatively stained and the goals of the single particle analysis are: (i) to enhance the SNR of the reconstructed protein granules by averaging the contrasts of selected protein granules; (ii) generate classes of protein granules based on the averaged contrasts; (iii) find the new structure of protein granules in averaged classes.

From the electron tomography analysis, two crystalline structures were observed, BCT and triclinic. It is thus questionable why the hIAPP protein granules do have a strong tendency to form the BCT and triclinic unit cells instead of any of the other twelve Bravais lattices? First, seen the weak binding force between the granules, it is surprising that the granules could form well ordered crystallites. Second, entities like in colloidal crystals built from

organic molecules that often interact by weak binding forces such as electrostatic forces crystallized in dense packed systems. All noble gases bind through weak van der Waals forces crystallized in the face centered cubic (FCC) structure. It is thus surprising that the granules are not crystallized in the densest packing order, which would result in FCC or hexagonal close packing (HCP) structures. The single particle analysis was applied to obtain more detailed structural information about protein granule to reach a better understanding of the driving force of the crystallization process.

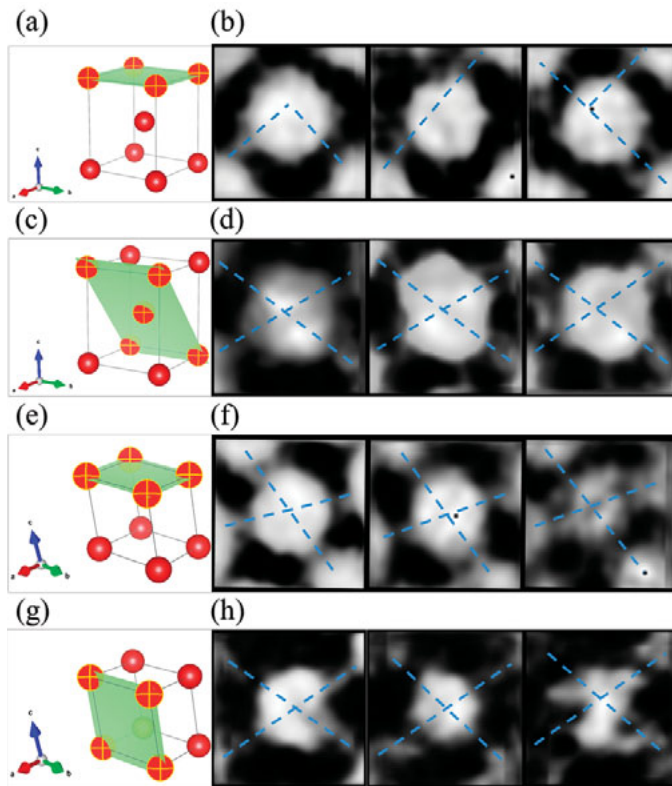


*Figure 26: Single particle analysis of the hIAPP protein granules. (a) and (c) show the layers parallel to the (001), and the (101) lattice planes were cut from the BCT unit cell, (b) and (d) are the three averaged classes from the selected particles from (a) and (c). (e) and (g) show the layers parallel to the (001), and (100) lattice planes that were cut from the triclinic unit cell, (f) and (h) are the three averaged classes from the selected particles from (e) and (g). The yellow cross marked particles in (a), (c), (e), and (g) indicate the protein granules selected for the single particle analysis. The dashed blue lines indicate the orientations of the linkers between the two nearest protein granules. Figure from the paper VI.*

For the single particle analysis, thin 20 nm slices were cut through the (001) and (101) lattice planes in the BCT structures and the (100) and (001) lattice planes in triclinic structures. 30 protein granules from each lattice plane were selected for single particle analysis. Merely translational alignment of boxed protein granules was applied in the 2D classification, thus an angle formed by two linkers was conserved in class-averaged particles. From the averaged classes, an intriguing finding is the filament like interconnection of hIAPP protein granules are discovered predominantly along the nearest neighbor directions as shown in **Figure 26**. The observation of the filaments connecting the hIAPP protein granules suggests the existence of the directional binding forces between two nearest protein granules in addition to dipole-dipole interactions taken so far to model the protein granule binding forces. These directional interconnecting filaments can explain the formation of the BCT and triclinic structures in the analyzed hIAPP protein aggregates.

### 5.3. Conclusion

Electron tomography technique revealed that the aggregates were made up of granular subunits aligned into a highly ordered structure in all three dimensions. The 3D lattice of hIAPP protein granules was constructed by two unit cells, as a BCT or a triclinic unit cell. A 5-fold twinned structure was observed by cyclic twinning of BCT and triclinic unit cells. The interaction between the two nearest hIAPP protein granules in both the unit cells is not only governed by the van der Waals forces but most likely also by filament like structures that connect the nearest neighbors. The multifunctional fat body tissue can be used for the storage of protein and also for detoxification. The observation of the crystalline structures of protein aggregation formed in this region should influence the lifespan of the *Drosophila melanogaster*.

## 6. Conclusions and outlook

The work presented in this doctoral thesis shows the importance of electron tomography technique for the understanding of nanostructural properties in selected hard and soft materials. The analysis results of the electron tomography have in this context shown to provide invaluable information to explain the formation mechanisms of the observed nanostructures and interfacial nanostructures.

### *Size measurement of Si NPs in 2D*

In the case of CVD deposited Si NPs, the average size of Si NPs measured from the reconstructed slices is smaller ( $\sim 0.8$  nm) than the value measured from the BFTEM image (discussed in **Chapter 4**). This is due to the overlapping effect, the smaller Si NPs can be sometimes completely or partially overlapped with larger ones in the 2D projections, thus the possibility of measuring the larger isolated NPs is higher than the smaller isolated ones. This leads to a biased sampling and results in an inaccurate size distribution of NPs measured from the 2D BFTEM images. The overlapping effect can be minimized by either preparing a very thin sample or the 3D density of NPs is too low to be considered as overlapped along the Z direction. When the sample thickness is comparable to the size of NPs, the relative homogeneous background and high contrast between the NPs and matrix makes it easy to automatically or manually measure the size of NPs (**Paper II**).

### *3D electron tomography*

In this thesis work, the applications of electron tomography on the hIAPP protein aggregates and the NP based absorber layer for third generation solar cells were demonstrated. The aggregation process of the amyloid polypeptides has a great impact on human health. All the amyloid-like structures observed in human *in vivo* are having a long fibrous morphology. In this thesis, a model system was applied to study the structure of hIAPP aggregates that are present in the fat body tissue surrounding the brain of *Drosophila melanogaster* (**Paper VI**). Electron tomography technique reveals the close to spherical morphology of hIAPP protein granules and the crystalline structures of the aggregates in three dimensions. For the first time, we could find the presence of a 5-fold twinned structure in biology that otherwise is only present in crystalline nanoparticles. An intriguing finding is the filament like interconnection of hIAPP protein granules observed predominantly along the nearest neighbor direction. The observation from single particle counting algorithms of the filaments connecting the hIAPP protein granules suggests the existence of the directional binding forces between two

nearest protein granules in addition to dipole-dipole interactions taking so far to model the protein granule binding forces. This observation thus shades new light on the aggregation mechanisms of amyloid polypeptides.

The BFTEM tomography was applied to investigate 3D density and spacing of Si NPs embedded in the ITO matrix (**Paper I**). From the reconstructed tomogram, the averaged spacing between the nearest NPs is measured to be 8.3 nm with a 3D density of  $1.6 \times 10^{18} \text{ cm}^{-3}$ . However, in the case of high temperature annealed SRSC film, BFTEM imaging is not sufficient to identify the c-Si and 3C-SiC NPs. EFTEM imaging using the low-loss signal has been demonstrated as a reliable technique to provide good contrast between Si and SiC phases. Thus, the EFTEM SI technique was chosen as the signal for the development of electron tomography. The routes towards fitting the reference spectra into the low-loss spectra (in a range of 12 eV to 26 eV) and reconstructing sub-volumes using the fitted plasmon signals have been highlighted in **Paper VII**. It has been the first time to show how the different phases, such as Si, a-SiC and 3C-SiC, are distributed in three dimensions in the annealed SRSC film. The formation of the interfacial nanostructure of a-SiC was explained in terms of thermodynamic concepts and indicates the nucleation and growth of 3C-SiC NPs does not reach the equilibrium condition after 1 hour annealing at 1100 °C. The methodology adopted to discover the interfacial nanostructure is believed not only limited to the high temperature annealed SRSC samples, but also more generally applicable to other material systems, such as alloys, that may have different plasmon energy losses in EELS.

#### *4D electron tomography*

The feasibility of developing 4D electron tomography using the low-loss signals (in a range of 12 eV to 30 eV) in EELS has been demonstrated in **Chapter 4.3**. In particular, the 4D dataset has been shown to provide valuable information in addition to conventional tomography dataset. The reconstructed spectra in the Si network region reveal the diffusion of C atoms into Si region, which could influence the crystallization process of Si during the annealing. More advanced statistical data treatment is in processing and expected to give full interpretation on the 4D “spectra-volume” dataset.

In conclusion, electron tomography is now an indispensable technique for both semiconductor materials characterization in materials science and also structural analysis for protein aggregates in life science. The information provided by electron tomography analysis can not be recovered by any other technique. Further developments are still necessary to improve the reliability of electron tomography technique.

## Acknowledgements

First of all, I would like to thank my supervisors: *Klaus*, thanks for opening a door for me into the electron microscopy field and your support and guidance through these years, your discussions and ideas have always been inspiring to me; *Stefano*, thanks for having the answers for all my questions and sharing with me the cultural differences between the regions of Scandinavia and Mediterranean Sea; *Håkan*, thanks for your interesting discussions on electron tomography.

To all my collaborators in “SNAPSUN” project: *Simon, Etienne, Stéphanie, Jérémy, Karol, René, Martijn, Shane, Hugh, Martyn, Jan and Vancho*, thanks for your research expertise and scientific work which are crucial for me to accomplish this work and the discussion with you has broadened my visions. Visiting to your research facilities was a great experience for me. *Lothar*, thanks for the arrangement and companionship during my research visit to Ernst Ruska-Centre at Juelich Research Centre.

To my collaborators from BMC: *Gunilla* and *Gu*, thanks for interesting discussions on fly modes and experimental results in the biologist’s point of view, and also for your quality feedbacks. Thanks to Dr. Daniel Primetzhofer for the ERDA measurement.

To my colleagues: *Tobias*, thanks for your accompany at lunch and coffee times; *Sultan*, thanks for your help on the experimental TEM; *Hasan J.*, thanks for sharing the knowledge in electronics at different length scales; *Tom*, thanks for the help on experimental TEM and tips for the data processing; *Timo*, thanks for the tips on the TEM sample preparation and experimental TEM; *Kathryn*, thanks for the tips on the electron tomography; *Sergej*, thanks for tips for the tomographic reconstruction; *Olivier*, thanks for the discussion and help on the TEM part; *Hasan A.*, thanks for the accompany at the TEM sample preparation room; *Hasan W.*, thanks for sharing the knowledge from your side as an office roommate; *Aqib*, thanks for joining the football team; *Hu*, thanks for the help during the ESEM lab; *Anumol and Sharath*, thanks for your accompany in the deep forest; *Yuanyuan*, thanks for sharing the NEWS during the lunch time; *Sylvester*, thanks to your nice



presentation in inter-cultural club; *Luimar*, thanks for introducing me the fish from the Amazon; *Max*, thanks for the local Swedish beers.

To all the support staff within *MSL* and the *Division of Applied Materials Science*, thank you for your assistance over the years. Thanks to the administration: Ingrid, Maria, Per and Sara for always helping out. Thanks to Jonatan for kind and efficient IT help.

To my dear friends: Sun Weiwei, Li Wei, Chu Jiangtao, Hai Ling, Hong Yue, Bai Wensong, Xiao Xin, Song Yang, Tian Yuan, thanks for your friendship and help. Special thanks to “Xiao Fan Zhuo” group. Thanks to all the buddies on the football field, especially, Adam, Philip, Liu Xijia and Bubu.

My deepest gratitude goes to *my families* for all their love and encouragement. Thanks to *my parents*, who raised me with a love of science and sacrificed their own lives to support me in all my pursuits. To my dear son, *Xie Hansheng*, keep the curiosities, you are so cute. The last word of acknowledgment is to my dear wife, *Yang Bo*, who has made these years the best time of my life.

Ling Xie

Uppsala, Sweden  
April, 2016

## Summary in Swedish

Analys av nanostrukturer som bildas i vissa material ger viktig information om morfologiska – och kemiska egenskaper, samt egenskaper vid gränssytor. Dessa är avgörande för att förstå ursprunget till tredje generationens solcellers elektriska egenskaper, samt samspelet mellan dessa och levande proteingranulat. I denna avhandling har nanostrukturer i två materialsystem analyserats. Nanopartikel (NP) baserade nanokompositer som används som absorberskikt för tredje generationens solceller och aggregering av aminosyran ”human Islet Amyloid Polypeptide” (hIAPP) i fettvävnaden av *Drosophila melanogaster*.

Använda syntesmetoder är kemisk ångavsättning (CVD), fysikalisk ångavsättning (PVD), aerosol-assisterad CVD (AACVD) och hög temperatur glödningsprocessen. Dessa användes för att utveckla tillverkningen av NP baserade absorberande skikt. För att förbättra transporten av laddningsbärrare i absorberande skikt, måste förhållandena vid syntestillverkningen av NP baserade absorberande skikt kontrolleras med önskvärda avstånd, samt densiteten hos NP i alla tre dimensioner. Detta motiverar utvecklingen av tredimensionella (3D) nano-karakteriseringstekniker för att studera 3D distribution av NP. Bland dessa NP baserade absorberande skikt, är 3D-fördelning av kisel (Si) NP som finns i kiselrika kiselkarbidfilmer (eng. SRSC-film), glödgade vid höga temperaturer, särskilt intressant på grund av de komplexa fasset separationsmekanismer som verkar.

Aggregeringsprocessen för hIAPP har en stor inverkan på människors hälsa, men en detaljerad analys av 3D-strukturen av hIAPP-aggregat saknas fortfarande. I denna avhandling har ett modellsystem tagits fram för att studera 3D-strukturen av hIAPP-aggregat som finns i fettvävnaden som omgärdar hjärnan av *Drosophila melanogaster*.

Termodynamiskt, delar bildandet av Si NP i kiselrika kiselkarbidfilmer (SRSC films) och uppträdandet av det olösliga ”human Islet Amyloid Polypeptide” (hIAPP) i vattenmiljö, den gemensamma utfällningsprocessen. På grund av att dimensionen hos fällningarna är i nanometerskala, har transmissionselektronmikroskopi (TEM) tillämpats som ett viktigt verktyg för att

analysera 3D-ordning och fördelning av fällningar, genom tekniken elektron-tomografi.

Electrontomografi är nu en vanligtvis använd teknik för 3D karakterisering på nanonivå. Dock är dess tillämpning i att korrelera komplexa 3D-nanostrukturer till uppkomstmekanismer fortfarande utmanande främst på grund av dålig kontrast och emellanåt otillräcklig upplösning. Till exempel, konventionella tvådimensionella (2D) TEM-avbildningstekniker, såsom ljusa fält bright field\_TEM (BFTEM) och hög upplöst TEM (HRTEM), är känsliga för kristallina NPar som är väl orienterade mot elektronstrålen. Vid jämförelse av kontrasten i bilder för NP i BFTEM eller HRTEM, med energi filtrerad TEM (EFTEM), kan EFTEM avbildningen upptäcka hela mängden av utfällda NPar. Således, är kontrasten i EFTEM bilder överlägsen BFTEM eller HRTEM bilder och valdes för utveckling av elektrontomografi. För första gången har data för sub- volymer av Si, amorft SiC (a-SiC) och kristallint kiselkarbid (3C-SiC) rekonstruerats med hjälp av EFTEM spektrum. Varken Si eller SiC fasar är helt kristalliserade efter en timmes glödning. En tunn amorf SiC-gränsyta (1 ~ 2 nm) observerades i 3D mellan ett strukturliknande Si-nätverk och kristallina kiselkarbid-NPar. Det strukturliknande Si-nätverket är en typisk morfologi av spinodalt sönderfallen Si-fas, medan bildningen av en SiC-gränsytan förklaras av utfällning av 3C-SiC NPar. Dessutom har möjligheterna med 4D-elektrontomografi visats med hjälp av EFTEM-data och det rekonstruerade elektronenergiförlustspektroskopi (EELS) spektrat i lägre förlustregionen (från 12 eV till 30 eV) visar förekomsten av kol (C) i Si-nätverkets struktur, som också detekterats med EELS SI i Scan TEM (STEM) läge med kärnförlustsignaler. Diffusionen av C-atomer i Si-regionen skulle kunna påverka kristallisationsprocessen av Si under glödning. Mer avancerad statistiska data är under bearbetning och förväntas ge en full tolkning av 4D "spektra-volym" datan.

Elektrontomografianalys av de hIAPP aggregaten som bildades i *Drosophila melanogaster* avslöjade att de stora aggregaten bestod utav granulära delenheter med en diameter av 20 nm ordnade i en starkt ordnad struktur i 3D. Den observerade kornstrukturen skiljer sig från den rapporterade fiberliknande amyloid strukturen, och anledningen till att 20 nm hIAPP granulat bildas är fortfarande oklar. 3D-gitter av hIAPP proteingranulat konstruerades med två enhetsceller, som en kroppcentrerad tetragonal (BCT) eller en triklinisk enhetscell. Det är första gången en 5-faldigt ihopvikt struktur upptäckts inom biologin; annars finns sådan struktur endast i kristallina nanopartiklar. Ett spännande fynd är glödtrådsliknande sammankopplingen av hIAPP proteingranulat som observerades, huvudsakligen i riktningen mot närmsta grannen. Observationen av trådarna som förbinder hIAPP proteingranulat tyder på förekomsten av riktningsbindningskrafter mellan de två närmaste proteingranulat utöver de krafter som kommer från från dipol-dipol interakt-

ioner hittills använts för att modellera proteingranulatbindningskrafter. Detta föreslår alltså nytt ljus på aggregerings mekanismer hos amyloid polypeptider.

Sammanfattningsvis är elektrontomografi nu en oersättlig teknik för både halvledarmaterialkaraktisering i materialvetenskap och strukturell analys för proteinaggregat inom life science. Informationen från elektrontomografi-analys kan inte fås av någon annan teknik. En fortsatta utvecklingen är dock fortfarande nödvändigt för att förbättra tillförlitligheten i elektrontomografi.

# Bibliography

1. Christian, J. W. in *The Theory of Transformations in Metals and Alloys* 718–796 (2002). doi:10.1016/B978-008044019-4/50021-0
2. Lifshitz, I. M. & Slyozov, V. V. THE KINETICS OF PRECIPITATION FROM SUPERSATURATED SOLID SOLUTIONS. *J. Phys. Chem. Solids* **19**, 35–50 (1961).
3. Trenberth, K. E., Dai, A., Rasmussen, R. M. & Parsons, D. B. The changing character of precipitation. *Bulletin of the American Meteorological Society* **84**, 1205–1217+1161 (2003).
4. Zellner, M. *et al.* Quantitative validation of different protein precipitation methods in proteome analysis of blood platelets. *Electrophoresis* **26**, 2481–2489 (2005).
5. Haass, C. & Selkoe, D. J. Soluble protein oligomers in neurodegeneration: lessons from the Alzheimer's amyloid beta-peptide. *Nat. Rev. Mol. Cell Biol.* **8**, 101–112 (2007).
6. Westermark, P., Engstrom, U., Johnson, K. H., Westermark, G. T. & Betsholtz, C. ISLET AMYLOID POLYPEPTIDE - PINPOINTING AMINO-ACID-RESIDUES LINKED TO AMYLOID FIBRIL FORMATION. *Proc. Natl. Acad. Sci. U. S. A.* **87**, 5036–5040 (1990).
7. British Petroleum. BP Statistical Review of World Energy, June 2014. *Nucl. Energy* www.bp.com/statisticalreview (2014). doi:10.2307/3324639
8. O'Gallagher, J. J. *Nonimaging Optics in Solar Energy. Synthesis Lectures on Energy and the Environment: Technology, Science, and Society* **2**, (2008).
9. *This was the Bell Labs' first 'Solar Battery.'* See Eric Wesoff, 'Happy 60th Anniversary to the Modern Solar Cell,' *Greentech Media*, 21 April 2014, <https://www.greentechmedia.com/articles/read/Happy-60th-Anniversary-to-the-Modern-Solar-Cell>.
10. Koenig, D., Rudd, J., Green, M. A. & Conibeer, G. Impact of interface on the effective band gap of Si quantum dots. *Sol. Energy Mater. Sol. Cells* **93**, 753–758 (2009).
11. Green, M. a. *Third generation photovoltaics: advanced solar energy conversion. Energy Conversion* **10**, (2006).
12. Conibeer, G. *et al.* Silicon quantum dot nanostructures for tandem photovoltaic cells. *Thin Solid Films* **516**, 6748–6756 (2008).
13. Yurtsever, A., Weyland, M. & Muller, D. A. Three-dimensional imaging of nonspherical silicon nanoparticles embedded in silicon oxide by plasmon tomography. *Appl. Phys. Lett.* **89**, (2006).
14. Nychyporuk, T. & Lemiti, M. Silicon-Based Third Generation Photovoltaics. *Sol. Cells-Silicon Wafer-Based Technol.* 139–176 (2011).
15. Cho, E. C. *et al.* Silicon quantum dots in a dielectric matrix for all-silicon tandem solar cells. *Adv. Optoelectron.* **2007**, (2007).

16. Roussel, M., Talbot, E., Pratibha Nalini, R., Gourbilleau, F. & Pareige, P. Phase transformation in SiO<sub>x</sub>/SiO<sub>2</sub> multilayers for optoelectronics and microelectronics applications. *Ultramicroscopy* **132**, 290–294 (2013).
17. Friedrich, D. *et al.* Sponge-like Si-SiO<sub>2</sub> nanocomposite-Morphology studies of spinodally decomposed silicon-rich oxide (vol 103, 131911, 2013). *Appl. Phys. Lett.* **103**, (2013).
18. Liedke, B., Heinig, K.-H., Mücklich, a. & Schmidt, B. Formation and coarsening of sponge-like Si-SiO<sub>2</sub> nanocomposites. *Appl. Phys. Lett.* **103**, 133106 (2013).
19. Müller, T., Heinig, K. H. & Möller, W. Size and location control of Si nanocrystals at ion beam synthesis in thin SiO<sub>2</sub> films. *Appl. Phys. Lett.* **81**, 3049–3051 (2002).
20. Müller, T. *et al.* Multi-dot floating-gates for nonvolatile semiconductor memories: Their ion beam synthesis and morphology. *Appl. Phys. Lett.* **85**, 2373–2375 (2004).
21. LaMer, V. & Dinegar, R. Theory, production and mechanism of formation of monodispersed hydrosols. *J. Am. Chem. ...* **72**, 4847–4854 (1950).
22. La Mer, V. K. Nucleation in Phase Transitions. *Ind. Eng. Chem.* **44**, 1270–1277 (1952).
23. Ostwald, W. Über die vermeintliche Isomerie des roten und gelben Quecksilberoxyds und die Oberflächenspannung fester Körper. *Zeitschrift für Phys. Chemie* **34**, 495–503 (1900).
24. Balluffi, R. W., Allen, S. M. & Carter, W. C. *Kinetics of Materials. Kinetics of Materials* (2005). doi:10.1002/0471749311
25. Bording, J. K. & Taftø, J. Molecular-dynamics simulation of growth of nanocrystals in an amorphous matrix. *Phys. Rev. B* **62**, 8098–8103 (2000).
26. Tartaj, P., Morales, M. a D. P., Veintemillas-Verdaguer, S., Gonz lez-Carre o, T. & Serna, C. J. The preparation of magnetic nanoparticles for applications in biomedicine. *J. Phys. D. Appl. Phys.* **36**, R182–R197 (2003).
27. Thanh, N. T. K., Maclean, N. & Mahiddine, S. Mechanisms of nucleation and growth of nanoparticles in solution. *Chem. Rev.* **114**, 7610–7630 (2014).
28. Bonafos, C. *et al.* Kinetic study of group IV nanoparticles ion beam synthesized in SiO<sub>2</sub>. *Nucl. Instruments Methods Phys. Res. Sect. B-Beam Interact. with Mater. Atoms* **178**, 17–24 (2001).
29. Kwon, S. G. & Hyeon, T. Formation mechanisms of uniform nanocrystals via hot-injection and heat-up methods. *Small* **7**, 2685–2702 (2011).
30. Cahn, J. W. ON SPINODAL DECOMPOSITION. *Acta Metall.* **9**, 795–801 (1961).
31. Miller, M. K. *et al.* Spinodal decomposition in Fe-Cr alloys: Experimental study at the atomic level and comparison with computer models—I. Introduction and methodology. *Acta Metall. Mater.* **43**, 3385–3401 (1995).
32. Seol, D. J. *et al.* Computer simulation of spinodal decomposition in constrained films. *Acta Mater.* **51**, 5173–5185 (2003).
33. Maley, N. & Lannin, J. S. Influence of hydrogen on vibrational and optical properties of aSiH alloys. *Phys. Rev. B* **36**, 1146–1152 (1987).
34. Hensel, J. C., Hasegawa, H. & Nakayama, M. Cyclotron resonance in uniaxially stressed silicon. II. Nature of the covalent bond. *Phys. Rev.* **138**, (1965).
35. Sohrabi, F., Nikniazi, A. & Movla, H. Optimization of Third Generation Nanostructured Silicon-Based Solar Cells. *Sol. Cells - Res. Appl. Perspect. - InTech* **1**, 1–26. do:10.5772/51616 (2013).

36. Song, D. *et al.* Fabrication and characterization of Si nanocrystals in SiC matrix produced by magnetron cosputtering. *J. Vac. Sci. Technol. B* **25**, 1327–1335 (2007).
37. Song, D. *et al.* Evolution of Si (and SiC) nanocrystal precipitation in SiC matrix. *Thin Solid Films* **516**, 3824–3830 (2008).
38. Kuenle, M., Janz, S., Nickel, K. G. & Eibl, O. Changes in chemical composition and nanostructure of SiC thin films prepared by PECVD during thermal annealing. *Phys. Status Solidi a-Applications Mater. Sci.* **208**, 1885–1895 (2011).
39. Kuenle, M. *et al.* Annealing of nm-thin Si<sub>1-x</sub>C<sub>x</sub>/SiC multilayers. *Sol. Energy Mater. Sol. Cells* **115**, 11–20 (2013).
40. Krauss, I. R., Merlino, A., Vergara, A. & Sica, F. An overview of biological macromolecule crystallization. *International Journal of Molecular Sciences* **14**, 11643–11691 (2013).
41. Chayen, N. E. Recent advances in methodology for the crystallization of biological macromolecules. *J. Cryst. Growth* **198-199**, 649–655 (1999).
42. Rhodes, G. Chapter 3 - Protein Crystals. *Crystallogr. Made Cryst. Clear* 31–47 (2006). doi:10.1016/B978-012587073-3/50005-2
43. Westermark, P. *et al.* A primer of amyloid nomenclature. *Amyloid* **14**, 179–183 (2007).
44. Ross, C. A. & Poirier, M. A. Opinion: What is the role of protein aggregation in neurodegeneration? *Nat. Rev. Mol. Cell Biol.* **6**, 891–8 (2005).
45. Chiti, F. & Dobson, C. M. Protein misfolding, functional amyloid, and human disease. *Annu. Rev. Biochem.* **75**, 333–66 (2006).
46. Sipe, J. D. & Cohen, A. S. Review: history of the amyloid fibril. *J. Struct. Biol.* **130**, 88–98 (2000).
47. Cohen, A. S. & Evan calkins. Electron Microscopic Observations on a Fibrous Component in Amyloid of Diverse Origins. *Nature* **183**, 1202–3 (1959).
48. Eanes, E. D. & Glenner, G. G. X-ray diffraction studies on amyloid filaments. *J. Histochem. Cytochem.* **16**, 673–677 (1968).
49. Iijima, K. *et al.* Dissecting the pathological effects of human Abeta40 and Abeta42 in Drosophila: a potential model for Alzheimer's disease. *Proc. Natl. Acad. Sci. U. S. A.* **101**, 6623–6628 (2004).
50. Crowther, D. C. *et al.* Intraneuronal Abeta, non-amyloid aggregates and neurodegeneration in a Drosophila model of Alzheimer's disease. *Neuroscience* **132**, 123–35 (2005).
51. Jackson, G. R. *et al.* Polyglutamine-expanded human huntingtin transgenes induce degeneration of Drosophila photoreceptor neurons. *Neuron* **21**, 633–642 (1998).
52. Bilen, J. & Bonini, N. M. Drosophila as a model for human neurodegenerative disease. *Annu. Rev. Genet.* **39**, 153–171 (2005).
53. Reiter, L. T., Potocki, L., Chien, S., Gribskov, M. & Bier, E. A systematic analysis of human disease-associated gene sequences in Drosophila melanogaster. *Genome Res.* **11**, 1114–25 (2001).
54. Chien, S., Reiter, L. T., Bier, E. & Gribskov, M. Homophila: human disease gene cognates in Drosophila. *Nucleic Acids Res.* **30**, 149–51 (2002).
55. Dobson, C. M. Principles of protein folding, misfolding and aggregation. in *Seminars in Cell and Developmental Biology* **15**, 3–16 (2004).
56. Olins, D. E. *et al.* Electron microscope tomography: transcription in three dimensions. *Science* **220**, 498–500 (1983).

57. Skoglund, U., Andersson, K., Strandberg, B. & Daneholt, B. Three-dimensional structure of a specific pre-messenger RNP particle established by electron microscope tomography. *Nature* **319**, 560–564 (1986).
58. Hoppe, W., Langer, R., Knesch, G. & Poppe, C. Protein-Kristallstrukturanalyse mit Elektronenstrahlen. *Naturwissenschaften* **55**, 333–336 (1968).
59. Hart, R. G. Electron Microscopy of Unstained Biological Material: The Polytopic Montage. *Science* (80-. ). **159**, 1464–1467 (1968).
60. De Rosier, D. J. & Klug, a. Reconstruction of Three Dimensional Structures from Electron Micrographs. *Nature* **217**, 130–134 (1968).
61. Dierksen, K., Typke, D., Hegerl, R. & Baumeister, W. Towards automatic electron tomography II. Implementation of autofocus and low-dose procedures. *Ultramicroscopy* **49**, 109–120 (1993).
62. Dierksen, K., Typke, D., Hegerl, R., Koster, A. J. & Baumeister, W. Towards automatic electron tomography. *Ultramicroscopy* **40**, 71–87 (1992).
63. Koster, a J., Chen, H., Sedat, J. W. & Agard, D. a. Automated microscopy for electron tomography. *Ultramicroscopy* **46**, 207–27 (1992).
64. Baumeister, W., Grimm, R. & Walz, J. Electron tomography of molecules and cells. *Trends in Cell Biology* **9**, 81–85 (1999).
65. Midgley, P. A. & Weyland, M. 3D electron microscopy in the physical sciences: The development of Z-contrast and EFTEM tomography. in *Ultramicroscopy* **96**, 413–431 (2003).
66. Midgley, P. a & Dunin-Borkowski, R. E. Electron tomography and holography in materials science. *Nat. Mater.* **8**, 271–280 (2009).
67. Kübel, C. *et al.* Recent advances in electron tomography: TEM and HAADF-STEM tomography for materials science and semiconductor applications. *Microsc. Microanal.* **11**, 378–400 (2005).
68. Möbus, G., Doole, R. C. & Inkson, B. J. Spectroscopic electron tomography. in *Ultramicroscopy* **96**, 433–451 (2003).
69. Möbus, G. & Inkson, B. J. Three-dimensional reconstruction of buried nanoparticles by element-sensitive tomography based on inelastically scattered electrons. *Appl. Phys. Lett.* **79**, 1369–1371 (2001).
70. Haberfehlner, G., Orthacker, A., Albu, M., Li, J. & Kothleitner, G. Nanoscale voxel spectroscopy by simultaneous EELS and EDS tomography. *Nanoscale* **6**, 14563–14569 (2014).
71. Kwon, O.-H. & Zewail, A. H. 4D electron tomography. *Science* (80-. ). **328**, 1668–1673 (2010).
72. Florea, I. *et al.* Analytical electron tomography mapping of the SiC pore oxidation at the nanoscale. *Nanoscale* **2**, 2668–2678 (2010).
73. Midgley, P. A., Weyland, M., Thomas, J. M. & Johnson, B. F. G. -Contrast tomography: a technique in three-dimensional nanostructural analysis based on Rutherford scattering. *Chem. Commun.* **0**, 907–908 (2001).
74. Brescia, R., Misztal, K., Dorfs, D., Manna, L. & Berton, G. Birth and growth of octapod-shaped colloidal nanocrystals studied by electron tomography. *J. Phys. Chem. C* **115**, 20128–20133 (2011).
75. Arslan, I., Tong, J. R. & Midgley, P. A. Reducing the missing wedge: High-resolution dual axis tomography of inorganic materials. *Ultramicroscopy* **106**, 994–1000 (2006).
76. Chuntanov, L., Bar-Sadan, M., Houben, L. & Haran, G. Correlating electron tomography and plasmon spectroscopy of single noble metal core-shell nanoparticles. *Nano Lett.* **12**, 145–150 (2012).



77. Benlekbiir, S., Epicier, T., Bausach, M., Aouine, M. & Berhault, G. STEM HAADF electron tomography of palladium nanoparticles with complex shapes. *Philos. Mag. Lett.* **89**, 145–153 (2009).
78. Bals, S. *et al.* Quantitative three-dimensional modeling of zeolite through discrete electron tomography. *J. Am. Chem. Soc.* **131**, 4769–4773 (2009).
79. Goris, B., Turner, S., Bals, S. & Van Tendeloo, G. Three-dimensional valency mapping in ceria nanocrystals. *ACS Nano* **8**, 10878–10884 (2014).
80. Jarausch, K., Thomas, P., Leonard, D. N., Twesten, R. & Booth, C. R. Four-dimensional STEM-EELS: Enabling nano-scale chemical tomography. *Ultramicroscopy* **109**, 326–337 (2009).
81. Nicoletti, O. *et al.* Three-dimensional imaging of localized surface plasmon resonances of metal nanoparticles. *Nature* **502**, 80–4 (2013).
82. Gass, M. H., Koziol, K. K. K., Windle, A. H. & Midgley, P. A. Four-dimensional spectral tomography of carbonaceous nanocomposites. *Nano Lett.* **6**, 376–379 (2006).
83. Linic, S., Christopher, P. & Ingram, D. B. Plasmonic-metal nanostructures for efficient conversion of solar to chemical energy. *Nat. Mater.* **10**, 911–921 (2011).
84. Etgar, L. Semiconductor nanocrystals as light harvesters in solar cells. *Materials* **6**, 445–459 (2013).
85. Tian, J. & Cao, G. Semiconductor quantum dot-sensitized solar cells. *Nano Rev.* **4**, 1–8 (2013).
86. Goubilleau, F., TERNON, C., Maestre, D., Palais, O. & Dufour, C. Silicon-rich SiO<sub>2</sub>/SiO<sub>2</sub> multilayers: A promising material for the third generation of solar cell. *J. Appl. Phys.* **106**, 13501 (2009).
87. Baron, T., Martin, F., Mur, P., Wyon, C. & Dupuy, M. Silicon quantum dot nucleation on Si<sub>3</sub>N<sub>4</sub>, SiO<sub>2</sub> and SiO<sub>x</sub>N<sub>y</sub> substrates for nanoelectronic devices. *J. Cryst. Growth* **209**, 1004–1008 (2000).
88. Quesnel, E., Pauliac-Vaujour, E. & Muffato, V. Modeling metallic nanoparticle synthesis in a magnetron-based nanocluster source by gas condensation of a sputtered vapor. *J. Appl. Phys.* **107**, (2010).
89. Tilley, R. D., Warner, J. H., Yamamoto, K., Matsui, I. & Fujimori, H. Micro-emulsion synthesis of monodisperse surface stabilized silicon nanocrystals. *Chem. Commun. (Camb)*. 1833–1835 (2005). doi:10.1039/b416069j
90. Barlow, F., Abdel Naby, M., Joshi, A. & Elshabini-Riad, A. Comprehensive evaluation of ITO thick films produced under optimum annealing conditions. *Sol. Energy Mater. Sol. Cells* **33**, 63–71 (1994).
91. Williams, D. B. & Carter, C. B. *Transmission Electron Microscopy: A Textbook for Materials Science. Materials Science V1-V4*, (2009).
92. Egerton, R. *Electron Energy-Loss Spectroscopy in the Electron Microscope. Book* (2011). doi:10.1007/978-1-4419-9583-4
93. Egerton, R. F. Electron energy-loss spectroscopy in the electron microscope. *Electron energy-loss Spectrosc. electron Microsc.* xii+410 pp–xii+410 pp (1986). at <<Go to ISI>://INSPEC:2876013>
94. Hofer, F., Grogger, W., Kothleitner, G. & Warbichler, P. Quantitative analysis of EFTEM elemental distribution images. *Ultramicroscopy* **67**, 83–103 (1997).
95. Schaffer, B., Kothleitner, G. & Grogger, W. EFTEM spectrum imaging at high-energy resolution. *Ultramicroscopy* **106**, 1129–1138 (2006).
96. Freitag, B. & Mader, W. Element specific imaging with high lateral resolution: An experimental study on layer structures. *J. Microsc.* **194**, 42–57 (1999).
97. Brydson, R. Electron Energy Loss Spectroscopy. *J. Alloys Compd.* **400**, 51–55 (2001).

98. Jeanguillaume, C. & Colliex, C. Spectrum-image: The next step in EELS digital acquisition and processing. *Ultramicroscopy* **28**, 252–257 (1989).
99. Ayache, J., Luc, B., Jacqueline, B., Gabrielle, E. & Daniele, L. *Sample Preparation Handbook for TRansmission Electron Microscopy Techniques*. (2010). doi:10.1007/978-0-387-98182-6
100. McCaffrey, J. P., Sullivan, B. T., Fraser, J. W. & Callahan, D. L. Use of transmitted color to calibrate the thickness of silicon samples. *Micron* **27**, 407–411 (1996).
101. McCaffrey, J. P. & Hulse, J. Transmitted color and interference fringes for TEM sample preparation of silicon. *Micron* **29**, 139–144 (1998).
102. Primak, W. Refractive index of silicon. *Appl. Opt.* **10**, 759–63 (1971).
103. Palgrave, R. G. & Parkin, I. P. Aerosol assisted chemical vapor deposition using nanoparticle precursors: A route to nanocomposite thin films. *J. Am. Chem. Soc.* **128**, 1587–1597 (2006).
104. Parola, S. *et al.* Structural properties of Ge nanocrystals synthesized by a PVD nanocluster source. *J. Nanoparticle Res.* **14**, (2012).
105. Parola, S., Quesnel, E., Muffato, V., Bartringer, J. & Slaoui, A. Influence of the embedding matrix on optical properties of Ge nanocrystals-based nanocomposite. *J. Appl. Phys.* **113**, (2013).
106. Schamm, S. *et al.* Imaging Si nanoparticles embedded in SiO<sub>2</sub> layers by (S)TEM-EELS. *Ultramicroscopy* **108**, 346–357 (2008).
107. Thomas, P. J. & Midgley, P. A. Image-spectroscopy-II. The removal of plural scattering from extended energy-filtered series by Fourier deconvolution. *Ultramicroscopy* **88**, 187–194 (2001).
108. Lawson, C. L. & Hanson, R. J. *Solving least squares problems. SIAM classics in applied mathematics* **15**, (1995).
109. Mitome, M., Yamazaki, Y., Takagi, H. & Nakagiri, T. SIZE DEPENDENCE OF PLASMON ENERGY IN SI CLUSTERS. *J. Appl. Phys.* **72**, 812–814 (1992).
110. Smit, C. *et al.* Determining the material structure of microcrystalline silicon from Raman spectra. *J. Appl. Phys.* **94**, 3582–3588 (2003).
111. Paillard, V. *et al.* Improved one-phonon confinement model for an accurate size determination of silicon nanocrystals. *J. Appl. Phys.* **86**, 1921 (1999).
112. Hawkes, P. W. in *Electron Tomography: Methods for Three-Dimensional Visualization of Structures in the Cell* 83–111 (2006). doi:10.1007/978-0-387-69008-7\_4
113. Bárcena, M. & Koster, A. J. Electron tomography in life science. *Semin. Cell Dev. Biol.* **20**, 920–930 (2009).
114. Howie, a. & Whelan, M. J. Diffraction Contrast of Electron Microscope Images of Crystal Lattice Defects. III. Results and Experimental Confirmation of the Dynamical Theory of Dislocation Image Contrast. *Proc. R. Soc. A Math. Phys. Eng. Sci.* **267**, 206–230 (1962).
115. Stadelmann, P. Image analysis and simulation software in transmission electron microscopy. *Microsc. Microanal.* **9**, 60–61 (2003).
116. Barnard, J. S., Sharp, J., Tong, J. R. & Midgley, P. a. High-resolution three-dimensional imaging of dislocations. *Science* **313**, 319 (2006).
117. Barnard, J. S., Eggeman, a. S., Sharp, J., White, T. a. & Midgley, P. a. Dislocation electron tomography and precession electron diffraction – minimising the effects of dynamical interactions in real and reciprocal space. *Philos. Mag.* **90**, 4711–4730 (2010).
118. Mastronarde, D. N. Dual-axis tomography: An approach with alignment methods that preserve resolution. *J. Struct. Biol.* **120**, 343–352 (1997).

119. Kawase, N., Kato, M., Nishioka, H. & Jinnai, H. Transmission electron microtomography without the ‘missing wedge’ for quantitative structural analysis. *Ultramicroscopy* **107**, 8–15 (2007).
120. Batenburg, K. J. *et al.* 3D imaging of nanomaterials by discrete tomography. *Ultramicroscopy* **109**, 730–740 (2009).
121. Goris, B., Van den Broek, W., Batenburg, K. J., Heidari Mezerji, H. & Bals, S. Electron tomography based on a total variation minimization reconstruction technique. *Ultramicroscopy* **113**, 120–130 (2012).
122. Owen, C. H. & Landis, W. J. Alignment of electron tomographic series by correlation without the use of gold particles. *Ultramicroscopy* **63**, 27–38 (1996).
123. Brandt, S., Heikkonen, J. & Engelhardt, P. Multiphase method for automatic alignment of transmission electron microscope images using markers. *J. Struct. Biol.* **133**, 10–22 (2001).
124. Starosolski, Z., Szczepanski, M., Wahle, M., Rusu, M. & Wriggers, W. Developing a denoising filter for electron microscopy and tomography data in the cloud. *Biophysical Reviews* **4**, 223–229 (2012).
125. Brandt, S. S. in *Electron Tomography: Methods for Three-Dimensional Visualization of Structures in the Cell* 187–215 (2006). doi:10.1007/978-0-387-69008-7\_7
126. Kobayashi, A., Fujigaya, T., Itoh, M., Taguchi, T. & Takano, H. Technical note: A tool for determining rotational tilt axis with or without fiducial markers. *Ultramicroscopy* **110**, 1–6 (2009).
127. Frank, J. *Three-Dimensional Electron Microscopy of Macromolecular Assemblies. Three-Dimensional Electron Microscopy of Macromolecular Assemblies* (1996). doi:10.1016/B978-012265040-6/50005-9
128. Johann Radon. Über die Bestimmung von Funktionen durch ihre Integralwerte längs gewisser Mannigfaltigkeiten. *Berichte der Sächsischen Akademie der Wiss.* **30**, 262–277 (1917).
129. Kak, A. & Slaney, M. in *Engineering* 344 (1988). doi:10.1137/1.9780898719277
130. Stark, H. & Woods, J. Direct Fourier reconstruction in computer tomography. *Acoust. Speech ...* **29**, 237–245 (1981).
131. Crowther, R. a., DeRosier, D. J. & Klug, a. The Reconstruction of a Three-Dimensional Structure from Projections and its Application to Electron Microscopy. *Proc. R. Soc. A Math. Phys. Eng. Sci.* **317**, 319–340 (1970).
132. Frank, J. *Electron tomography: Methods for three-dimensional visualization of structures in the cell. Electron Tomography: Methods for Three-Dimensional Visualization of Structures in the Cell* (2006). doi:10.1007/978-0-387-69008-7
133. Gilbert, P. Iterative methods for the three-dimensional reconstruction of an object from projections. *J. Theor. Biol.* **36**, 105–117 (1972).
134. Gordon, R., Bender, R. & Herman, G. T. Algebraic reconstruction techniques (ART) for three-dimensional electron microscopy and x-ray photography. *J. Theor. Biol.* **29**, 471–481 (1970).
135. Black, M. J., Sapiro, G., Marimont, D. H. & Heeger, D. Robust anisotropic diffusion. *IEEE Trans. Image Process.* **7**, 421–432 (1998).
136. Weickert, J., Ter Haar Romeny, B. M. & Viergever, M. A. Efficient and reliable schemes for nonlinear diffusion filtering. *IEEE Trans. Image Process.* **7**, 398–410 (1998).
137. IMOD homepage. <http://bio3d.colorado.edu/imod/>.
138. Kremer, J. R., Mastronarde, D. N. & McIntosh, J. R. Computer visualization of three-dimensional image data using IMOD. *J. Struct. Biol.* **116**, 71–76 (1996).

139. Olesinski, R. W. & Abbaschian, G. J. The C-Si (Carbon-Silicon) system. *Bull. Alloy Phase Diagrams* **5**, 486–489 (1984).
140. Hoppe, W., Schramm, H. J., Sturm, M., Hunsmann, N. & Gaßmann, J. Three-Dimensional Electron Microscopy of Individual Biological Objects Part III. Experimental Results on Yeast Fatty Acid Synthetase. *Zeitschrift für Naturforsch. - Sect. A J. Phys. Sci.* **31**, 1380–1390 (1976).
141. McEwen, B. F. & Marko, M. The emergence of electron tomography as an important tool for investigating cellular ultrastructure. *J. Histochem. Cytochem.* **49**, 553–563 (2001).
142. Westermark, P. *et al.* Amyloid fibrils in human insulinoma and islets of Langerhans of the diabetic cat are derived from a neuropeptide-like protein also present in normal islet cells. *Proc. Natl. Acad. Sci. U. S. A.* **84**, 3881–5 (1987).
143. Prüßing, K., Voigt, A. & Schulz, J. B. *Drosophila melanogaster* as a model organism for Alzheimer's disease. *Mol. Neurodegener.* **8**, 35 (2013).
144. Norlin, N. *et al.* Aggregation and fibril morphology of the Arctic mutation of Alzheimer's A $\beta$  peptide by CD, TEM, STEM and in situ AFM. *J. Struct. Biol.* **180**, 174–189 (2012).
145. Raman, C. Electron microscopy and immunogold labelling analysis of smart nano- particles ( storage proteins ) in insects. 167–178 (2012).
146. Rizki, T. M. & Rizki, R. M. LARVAL ADIPOSE-TISSUE OF HOMOEOTIC BITHORAX MUTANTS OF DROSOPHILA. *Dev. Biol.* **65**, 476–482 (1978).
147. Roma, G. C., Bueno, O. C. & Camargo-Mathias, M. I. Morpho-physiological analysis of the insect fat body: A review. *Micron* **41**, 395–401 (2010).
148. Schultz, S. W., Nilsson, K. P. R. & Westermark, G. T. *Drosophila melanogaster* as a model system for studies of islet amyloid polypeptide aggregation. *PLoS One* **6**, (2011).
149. Walz, J. *et al.* Tricorn protease exists as an icosahedral supermolecule in vivo. *Mol. Cell* **1**, 59–65 (1997).
150. Orlova, E. V. & Saibil, H. R. Structural analysis of macromolecular assemblies by electron microscopy. *Chemical Reviews* **111**, 7710–7748 (2011).
151. Cheng, Y. & Walz, T. The advent of near-atomic resolution in single-particle electron microscopy. *Annu. Rev. Biochem.* **78**, 723–742 (2009).
152. Grigorieff, N. & Harrison, S. C. Near-atomic resolution reconstructions of icosahedral viruses from electron cryo-microscopy. *Current Opinion in Structural Biology* **21**, 265–273 (2011).
153. Zhang, X. *et al.* Near-atomic resolution using electron cryomicroscopy and single-particle reconstruction. *Proc. Natl. Acad. Sci. U. S. A.* **105**, 1867–72 (2008).
154. Adrian, M., Dubochet, J., Lepault, J. & McDowell, A. W. Cryo-electron microscopy of viruses. *Nature* **308**, 32–36 (1984).
155. Elmlund, D. & Elmlund, H. Cryogenic electron microscopy and single-particle analysis. *Annu. Rev. Biochem.* **84**, 499–517 (2015).
156. Grigorieff, N. FREALIGN: High-resolution refinement of single particle structures. *J. Struct. Biol.* **157**, 117–125 (2007).



# Acta Universitatis Upsaliensis

*Digital Comprehensive Summaries of Uppsala Dissertations  
from the Faculty of Science and Technology 1380*

Editor: The Dean of the Faculty of Science and Technology

A doctoral dissertation from the Faculty of Science and Technology, Uppsala University, is usually a summary of a number of papers. A few copies of the complete dissertation are kept at major Swedish research libraries, while the summary alone is distributed internationally through the series Digital Comprehensive Summaries of Uppsala Dissertations from the Faculty of Science and Technology. (Prior to January, 2005, the series was published under the title "Comprehensive Summaries of Uppsala Dissertations from the Faculty of Science and Technology".)



ACTA  
UNIVERSITATIS  
UPSALIENSIS  
UPPSALA  
2016

Distribution: [publications.uu.se](http://publications.uu.se)  
urn:nbn:se:uu:diva-284102